MONKES: a fast neoclassical code for the evaluation of monoenergetic transport coefficients

F. J. Escoto[1], J. L. Velasco[1], I. Calvo[1], M. Landreman[2] and F. I. Parra[3]

[1]Laboratorio Nacional de Fusión, CIEMAT, 28040 Madrid, Spain
[2]University of Maryland, College Park, MD 20742, USA
[3]Princeton Plasma Physics Laboratory, Princeton, NJ 08540, USA

E-mail: `fjavier.escoto@ciemat.es`

April 2023

Abstract. The bootstrap current needs to be addressed in the optimization of stellarator configurations. However, its computation is usually too slow to be evaluated at each iteration of the optimization process. `MONKES` is a new neoclassical code for the fast evaluation of monoenergetic transport coefficients in large aspect ratio stellarators. By means of a convergence study at low collisionality and benchmarks with other codes, it is shown that `MONKES` is accurate and efficient. The combination of spectral discretization in spatial and velocity coordinates with block sparsity allows `MONKES` to compute monoenergetic coefficients at low collisionality, in a single processor, in approximately one minute. These features make `MONKES` ideally suited for its inclusion in stellarator optimization codes and transport suites.

Keywords: stellarator optimization, neoclassical transport, bootstrap current.
Submitted to: *Nucl. Fusion*

1. Introduction

Stellarators are an attractive alternative to tokamaks as future fusion reactors. While tokamaks require a large toroidal current to generate part of the magnetic field, stellarators can create it entirely by external magnets. As a consequence, stellarators avoid current-induced instabilities and facilitate the steady-state operation. These advantages come at the expense of making the magnetic field three-dimensional. In tokamaks, axisymmetry guarantees that the radial displacement that charged particles experience along their collisionless orbits averages to zero. Therefore, in the absence of collisions, all charged particles are confined. However, in a generic stellarator there is an outwards secular radial movement and particles quickly drift out of the device. Such combination of a non zero orbit-averaged radial drift and a small collision frequency (the relevant scenario for fusion plasmas) produces, for a generic stellarator, intolerably large levels of neoclassical transport.

Hence, stellarator magnetic fields must be carefully designed in order to display good confinement properties. This process of tailoring of the magnetic field is called stellarator optimization. The goal of neoclassical optimization is to obtain a stellarator with levels of neoclassical losses equivalent or lower to those in an axisymmetric device. Stellarator magnetic fields in which the orbit-averaged radial magnetic drift is zero for all particles are called omnigenous [5]. Thus, the goal of neoclassical optimization is to obtain magnetic fields which are close to omnigeneity. However, addressing only radial transport in the optimization process is not sufficient. In toroidal plasmas, the parallel flow of electrons and the rest of species is not, in general, balanced. This mismatch produces a net parallel current at each flux surface which, through Ampère's law, modifies the magnetic field $\boldsymbol{B}$. When the current is generated by neoclassical mechanisms and non-zero plasma profile gradients, we speak of bootstrap current. The bootstrap current and its effect on the magnetic configuration must be taken into account in the design of optimized stellarator magnetic fields.

Two different subclasses of omnigenous stellarators have drawn particular attention: quasi-isodynamic (QI) and quasi-symmetric (QS) stellarators. Quasi-isodynamic configurations have the additional property (besides omnigeneity) that contour lines of constant magnetic field strength $B := |\boldsymbol{B}|$ in a flux surface close poloidally. This additional constraint has an important implication: QI stellarators produce zero bootstrap current at low collisionality [6, 7]. Thanks to this feature, QI stellarators can control plasma-wall interaction by means of a divertor relying on a specific structure of islands, which cannot be realized in the presence of toroidal currents. The Wendelstein 7-X (W7-X) experiment was designed to be close to QI and demonstrates that theoretically based stellarator optimization can be applied to construct a device with much better confinement properties than any previous stellarator [8]. Despite its success, there is still room for improvement. The two principal configurations of W7-X, the KJM or so-called "high mirror" and the EIM also known as "standard" are not optimized for simultaneously having low levels of radial and parallel transport [9]. Consequently, optimization of QI stellarators is a very active branch of research and enormous effort has been put in pushing forward the design and construction of quasi-isodynamic stellarators [10, 11, 12, 13, 14].

The QS subclass of omnigenous configurations is attractive as the neoclassical properties of such magnetic fields are isomorphic to those in a tokamak [15, 16]. It has been shown that it is possible to design QS magnetic fields with extremely low neoclassical losses [17]. In contrast to QI configurations, QS stellarators are expected to have a substantial bootstrap current‡. Examples of this subclass are the Helically Symmetric eXperiment (HSX) [18] or the unfinished National Compact Stellarator Experiment (NCSX) [19].

At each iteration of the optimization process it is necessary to evaluate a large number ($\sim 10^2$) of magnetic configurations. Therefore, in order to neoclassically optimize a magnetic field it is required to be able to evaluate fast the neoclassical properties of each configuration. Due to this requirement, neoclassical properties are typically addressed indirectly. One example of addressing indirectly neoclassical properties comes from knowing that in an omnigenous stellarator local maxima and minima of B along field lines are aligned. Therefore, it seems reasonable to try to align these extrema in neoclassical optimization. Another example is to optimize pursuing that the isolines of B close poloidally in a flux surface, hoping to achieve quasi-isodynamicity. A different manner to address indirectly neoclassical properties is through figures of merit for the collisional regime of interest. For the $1/\nu$ regime, the code `NEO` [20] computes the effective ripple ϵ_{eff}, which encapsulates the dependence on the magnetic configuration of radial neoclassical transport. For transport within the flux surface, there exist long mean free path formulae for parallel flow and bootstrap current [24, 25, 26]. Although they can be computed very fast and might capture some qualitative behaviour, these formulae are plagued with noise due to resonances in rational surfaces and even with

‡ With the exception of the quasi-poloidally symmetric magnetic field, which lies at the intersection of QI and QS configurations. However, this configuration is magnetohydrodynamically unstable at the core.

smoothing ad-hoc techniques, they are not accurate [27]. This lack of accuracy limits their application for optimization purposes. During the optimization process, an accurate calculation of the bootstrap current is required to account for its effect (e.g. for optimizing QS stellarators) or to keep it sufficiently small (when optimizing for quasi-isodinamicity).

Recent developments allow direct optimization of radial neoclassical transport. Based on rigorous derivations [3, 4], the code `KNOSOS` [21, 22] solves very fast an orbit-averaged drift-kinetic equation that is accurate for low collisionality regimes. `KNOSOS` is included in the stellarator optimization suite `STELLOPT` [23].

In this work we present `MONKES` (MONoenergetic Kinetic Equation Solver), a new neoclassical code conceived to satisfy the necessity of taking into account the bootstrap current effect in stellarator optimization suites. Specifically, `MONKES` makes it possible to include in the optimization targets the monoenergetic coefficients $\widehat{D}_{ij}$ $i,j \in \{1,2,3\}$ (their precise definition is given in section 2). These nine coefficients encapsulate the neoclassical transport across and within the flux surface. The coefficients $\widehat{D}_{ij}$ for $i \in \{1,2\}$ allow to compute the flux of particles and heat across the flux surface. For transport within the flux surface, the parallel flow of each species can be calculated in terms of the coefficients $\widehat{D}_{3j}$. In the absence of externally applied loop voltage, the bootstrap current is driven by the radial electric field and gradients of density and temperature. The so-called bootstrap current coefficient $\widehat{D}_{31}$ is the one that relates the parallel flow to these gradients. As it also computes fast the radial transport coefficients, as a corollary, it will allow to optimize taking into account the $1/\nu$ to plateau transition. Apart from optimization, `MONKES` can find many other applications. For instance, it can be used for the analysis of experimental discharges or also be included in predictive transport frameworks such as `TANGO` [29] and `TRINITY` [30].

This paper is organized as follows: in section 2, we introduce the drift-kinetic equation solved by `MONKES` and the transport coefficients that it computes. In section 3, we explain the algorithm used to solve the drift-kinetic equation and its implementation. In section 4, by means of a convergence study, we demonstrate that `MONKES` can be used to compute accurate monoenergetic coefficients at low collisionality very fast for the $1/\nu$ and $\sqrt{\nu}$ regimes. `MONKES` results are also benchmarked against `DKES` [31] and, when necessary, against `SFINCS` [32]. Finally, in section 5 we summarize the results and discuss future lines of work.

2. Drift-kinetic equation and transport coefficients

`MONKES` solves the drift-kinetic equation

$$(v\xi \boldsymbol{b} + \boldsymbol{v}_E)\cdot\nabla h_a + v\nabla\cdot\boldsymbol{b}\frac{(1-\xi^2)}{2}\frac{\partial h_a}{\partial \xi} - \nu^a \mathcal{L} h_a = S_a, \quad (1)$$

where $\boldsymbol{b} := \boldsymbol{B}/B$ is the unitary vector tangent to magnetic field lines and we have employed as velocity coordinates the cosine of the pitch-angle $\xi := \boldsymbol{v}\cdot\boldsymbol{b}/|\boldsymbol{v}|$ and the magnitude of the velocity $v := |\boldsymbol{v}|$.

We assume that the magnetic configuration has nested flux surfaces. We denote by $\psi \in [0, \psi_{\rm lcfs}]$ a radial coordinate that labels flux surfaces, where $\psi_{\rm lcfs}$ denotes the label of the last closed flux surface. In equation (1), h_a is the non-adiabatic component of the deviation of the distribution function from a local Maxwellian for a plasma species a

$$f_{{\rm M}a}(\psi, v) := n_a(\psi)\pi^{-3/2} v_{{\rm t}a}^{-3}(\psi)\exp\left(-\frac{v^2}{v_{{\rm t}a}^2(\psi)}\right). \quad (2)$$

Here, n_a is the density of species a, $v_{{\rm t}a} := \sqrt{2T_a/m_a}$ is its thermal velocity, T_a its temperature (in energy units) and m_a its mass.

For the convective term in equation (1)

$$\boldsymbol{v}_E := \frac{\boldsymbol{E}_0\times\boldsymbol{B}}{\langle B^2\rangle} = -E_\psi(\psi)\frac{\boldsymbol{B}\times\nabla\psi}{\langle B^2\rangle} \quad (3)$$

denotes the incompressible $\boldsymbol{E}\times\boldsymbol{B}$ drift approximation and $\boldsymbol{E}_0 = E_\psi(\psi)\nabla\psi$ is the piece of the electric field $\boldsymbol{E}$ perpendicular to the flux surface. The symbol $\langle ...\rangle$ stands for the flux surface average operation. We denote the Lorentz pitch-angle scattering operator by $\mathcal{L}$, which in coordinates (ξ, v) takes the form

$$\mathcal{L} = \frac{1}{2}\frac{\partial}{\partial\xi}\left((1-\xi^2)\frac{\partial}{\partial\xi}\right). \quad (4)$$

In the collision operator, $\nu^a(v) = \sum_b \nu^{ab}(v)$ and

$$\nu^{ab}(v) := \frac{4\pi n_b e_a^2 e_b^2}{m_a^2 v_{{\rm t}a}^3}\log\Lambda\frac{{\rm erf}(v/v_{{\rm t}b}) - G(v/v_{{\rm t}b})}{v^3/v_{{\rm t}a}^3} \quad (5)$$

stands for the pitch-angle collision frequency between species a and b. We denote the Chandrasekhar function by $G(x) = \left[{\rm erf}(x) - (2x/\sqrt{\pi})\exp(-x^2)\right]/(2x^2)$, ${\rm erf}(x)$ is the error function and $\log\Lambda$ is the Coulomb logarithm [33].

On the right-hand-side of equation (1)

$$S_a := -\boldsymbol{v}_{{\rm m}a}\cdot\nabla\psi\left(A_{1a} + \frac{v^2}{v_{{\rm t}a}^2}A_{2a}\right)f_{{\rm M}a} + Bv\xi A_{3a} f_{{\rm M}a} \quad (6)$$

is the source term,

$$\boldsymbol{v}_{\mathrm{m}a}\cdot\nabla\psi = -\frac{Bv^2}{\Omega_a}\frac{1+\xi^2}{2B^3}\boldsymbol{B}\times\nabla\psi\cdot\nabla B \tag{7}$$

is the expression of the radial magnetic drift assuming ideal magnetohydrodynamical equilibrium, $\Omega_a = e_aB/m_a$ is the gyrofrecuency of species a, e_a its charge and the flux functions

$$A_{1a}(\psi) := \frac{\mathrm{d}\ln n_a}{\mathrm{d}\psi} - \frac{3}{2}\frac{\mathrm{d}\ln T_a}{\mathrm{d}\psi} - \frac{e_aE_\psi}{T_a}, \tag{8}$$

$$A_{2a}(\psi) := \frac{\mathrm{d}\ln T_a}{\mathrm{d}\psi}, \tag{9}$$

$$A_{3a}(\psi) := \frac{e_a}{T_a}\frac{\langle\boldsymbol{E}\cdot\boldsymbol{B}\rangle}{\langle B^2\rangle}, \tag{10}$$

are the so-called thermodinamical forces.

The solution to equation (1) is determined up to an additive function $g(\psi, v)$. This function is unimportant as it does not contribute to the transport coefficients. Nevertheless, in order to have a unique solution to the drift-kinetic equation, it must be fixed by imposing an appropriate additional constraint. We will select this free function (for fixed (ψ, v)) by imposing

$$\left\langle\int_{-1}^{1} h_a\,\mathrm{d}\xi\right\rangle = C, \tag{11}$$

for some $C\in\mathbb{R}$ that will be determined indirectly.

The drift-kinetic equation (1) is the one presented in [34]. An equivalent form of this equation is solved by the standard neoclassical code `DKES` [31] using a variational principle.

Taking the moments $\{\boldsymbol{v}_{\mathrm{m}a}\cdot\nabla\psi, (v^2/v_{ta}^2)\boldsymbol{v}_{\mathrm{m}a}\cdot\nabla\psi, v\xi B\}$ of h_a and then the flux-surface average yields, respectively, the radial particle flux, the radial heat flux and the parallel flow

$$\langle\boldsymbol{\Gamma}_a\cdot\nabla\psi\rangle := \left\langle\int \boldsymbol{v}_{\mathrm{m}a}\cdot\nabla\psi\; h_a\,\mathrm{d}^3\boldsymbol{v}\right\rangle, \tag{12}$$

$$\left\langle\frac{\boldsymbol{Q}_a\cdot\nabla\psi}{T_a}\right\rangle := \left\langle\int \frac{v^2}{v_{ta}^2}\boldsymbol{v}_{\mathrm{m}a}\cdot\nabla\psi\; h_a\,\mathrm{d}^3\boldsymbol{v}\right\rangle, \tag{13}$$

$$\langle n_a\boldsymbol{V}_a\cdot\boldsymbol{B}\rangle := \left\langle B\int v\xi\; h_a\,\mathrm{d}^3\boldsymbol{v}\right\rangle. \tag{14}$$

It is a common practice for linear drift-kinetic equations (e.g. [34], [2], [32]) to apply superposition and split h_a in three additive terms. Each one of them is a solution to the drift-kinetic equation using as source one of the three summands of the right hand side of definition (6). Besides, as in the drift-kinetic equation (1) there are no derivatives or integrals along ψ nor v, it is convenient to use the splitting

$$h_a = f_{\mathrm{M}a}\left[\frac{Bv}{\Omega_a}\left(A_{1a}f_1 + A_{2a}\frac{v^2}{v_{ta}^2}f_2\right) + A_{3a}f_3\right], \tag{15}$$

relating h_a to three functions $\{f_j\}_{j=1}^3$. The splitting is chosen so that the functions $\{f_j\}_{j=1}^3$ are solutions to

$$\xi\boldsymbol{b}\cdot\nabla f_j + \nabla\cdot\boldsymbol{b}\frac{(1-\xi^2)}{2}\frac{\partial f_j}{\partial\xi} - \frac{\hat{E}_\psi}{\langle B^2\rangle}\boldsymbol{B}\times\nabla\psi\cdot\nabla f_j - \hat{\nu}\mathcal{L}f_j = s_j, \tag{16}$$

for $j=1,2,3$, where $\hat{\nu} := \nu(v)/v$ and $\hat{E}_\psi := E_\psi/v$. The source terms are defined as

$$s_1 := -\boldsymbol{v}_{\mathrm{m}a}\cdot\nabla\psi\frac{\Omega_a}{Bv^2}, \quad s_2 := s_1, \quad s_3 := \xi B. \tag{17}$$

The relation between h_a and f_j given by equation (15) is such that the transport quantities (12), (13) and (14) can be written in terms of three transport coefficients which for fixed $(\hat{\nu}, \hat{E}_\psi)$ depend only on the magnetic configuration. As $\mathrm{d}\hat{\nu}/\mathrm{d}v$ never annuls, the dependence of f_j on the velocity v can be parametrized by its dependence on $\hat{\nu}$. Thus, for fixed $(\hat{\nu}, \hat{E}_\psi)$, equation (16) is completely determined by the magnetic configuration. Hence, its unique solutions f_j that satisfy condition (11) are also completely determined by the magnetic configuration. The ad-hoc assumptions that lead to ψ and v appearing as mere parameters in the drift-kinetic equation (1) comprise the so called monoenergetic approximation to neoclassical transport (see e.g. [35]).

Using (15) we can write the transport quantities (12), (13) and (14) in terms of the Onsager matrix

$$\begin{bmatrix} \langle\boldsymbol{\Gamma}_a\cdot\nabla\psi\rangle \\ \left\langle\frac{\boldsymbol{Q}_a\cdot\nabla\psi}{T_a}\right\rangle \\ \langle n_a\boldsymbol{V}_a\cdot\boldsymbol{B}\rangle \end{bmatrix} = \begin{bmatrix} L_{11a} & L_{12a} & L_{13a} \\ L_{21a} & L_{22a} & L_{23a} \\ L_{31a} & L_{32a} & L_{33a} \end{bmatrix}\begin{bmatrix} A_{1a} \\ A_{2a} \\ A_{3a} \end{bmatrix}. \tag{18}$$

We have defined the thermal transport coefficients as

$$L_{ija} := \int_0^\infty 2\pi v^2 f_{\mathrm{M}a} w_i w_j D_{ija}\,\mathrm{d}v\,, \tag{19}$$

where $w_1 = w_3 = 1$, $w_2 = v^2/v_{ta}^2$ and we have used that $\int g\,\mathrm{d}^3\boldsymbol{v} = 2\pi\int_0^\infty\int_{-1}^1 gv^2\,\mathrm{d}\xi\,\mathrm{d}v$ for any integrable function $g(\xi, v)$. The quantities D_{ija} are the monoenergetic transport coefficients, defined as

$$D_{ija} := \frac{B^2v^3}{\Omega_a^2}\widehat{D}_{ij}, \qquad i,j\in\{1,2\}, \tag{20}$$

$$D_{i3a} := \frac{Bv^2}{\Omega_a}\widehat{D}_{i3}, \qquad i\in\{1,2\}, \tag{21}$$

$$D_{3ja} := \frac{Bv^2}{\Omega_a}\widehat{D}_{3j}, \qquad j\in\{1,2\}, \tag{22}$$

$$D_{33a} := v\widehat{D}_{33}, \tag{23}$$

and $\widehat{D}_{ij}$ are the monoenergetic geometric coefficients

$$\widehat{D}_{ij}(\psi, v) := \left\langle\int_{-1}^{1} s_i f_j\,\mathrm{d}\xi\right\rangle, \quad i,j\in\{1,2,3\}. \tag{24}$$

Note that, unlike D_{ija}, the monoenergetic geometric coefficients $\widehat{D}_{ij}$ do not depend on the species for fixed $\hat{\nu}$ (however the correspondent value of v associated to each $\hat{\nu}$ varies between species) and depend only on the magnetic geometry. Of the monoenergetic geometric coefficients $\widehat{D}_{ij}$ only three of them are independent as Onsager symmetry implies $\widehat{D}_{13} = \widehat{D}_{31}$. Hence, obtaining the transport coefficients for all species requires to solve (16) for two different source terms s_1 and s_3. The algorithm for solving equation (16) is described in the next section.

3. Numerical method

In this section we describe the algorithm implemented to numerically solve the drift-kinetic equation (16). We drop the subscript j from that labels every different source term. Also, as ψ and v act as mere parameters we will omit their dependence in this section and functions of these two variables will be referred as constants. First, in subsection 3.1 we will present the algorithm in a formal and abstract manner which is valid for any set of spatial coordinates. The algorithm, based on the tridiagonal representation of the drift-kinetic equation, merges naturally when discretizing the velocity coordinate ξ using a Legendre spectral method. Nevertheless, for convenience, we will explain it in (right-handed) Boozer coordinates $(\psi, \theta, \zeta) \in [0, \psi_{\text{lcfs}}] \times [0, 2\pi) \times [0, 2\pi/N_p)$. In these coordinates $2\pi\psi$ is the toroidal flux of the magnetic field and θ, ζ are respectively the poloidal and toroidal (in a single period) angles. The integer $N_p \geq 1$ denotes the number of periods of the device. In Boozer coordinates the magnetic field can be written as

$$\begin{aligned}\boldsymbol{B} &= \nabla\psi \times \nabla\theta - \iota(\psi)\nabla\psi \times \nabla\zeta \\ &= B_\psi(\psi,\theta,\zeta)\nabla\psi + B_\theta(\psi)\nabla\theta + B_\zeta(\psi)\nabla\zeta, \end{aligned} \tag{25}$$

and the Jacobian of the transformation reads

$$\sqrt{g}(\psi,\theta,\zeta) := (\nabla\psi \times \nabla\theta \cdot \nabla\zeta)^{-1} = \frac{B_\zeta + \iota B_\theta}{B^2}, \tag{26}$$

where $\iota := \boldsymbol{B} \cdot \nabla\theta / \boldsymbol{B} \cdot \nabla\zeta$ is the rotational transform. Using (25) and (26), the spatial differential operators present in the drift-kinetic equation (16) can be expressed in these coordinates as

$$\boldsymbol{b} \cdot \nabla = \frac{B}{B_\zeta + \iota B_\theta}\left(\iota\frac{\partial}{\partial\theta} + \frac{\partial}{\partial\zeta}\right), \tag{27}$$

$$\boldsymbol{B} \times \nabla\psi \cdot \nabla = \frac{B^2}{B_\zeta + \iota B_\theta}\left(B_\zeta\frac{\partial}{\partial\theta} - B_\theta\frac{\partial}{\partial\zeta}\right). \tag{28}$$

After the abstract explanation of the algorithm, in subsection 3.2 we explain how is implemented in `MONKES`.

3.1. Legendre polynomial expansion

The algorithm is based on the approximate representation of the distribution function f in a truncated Legendre series. We will search for approximate solutions to equation (16) of the form

$$f(\theta,\zeta,\xi) = \sum_{k=0}^{N_\xi} f^{(k)}(\theta,\zeta)P_k(\xi), \tag{29}$$

where $f^{(k)} = \langle f, P_k\rangle_{\mathcal{L}} / \langle P_k, P_k\rangle_{\mathcal{L}}$ is the $k-$th Legendre mode of $f(\theta,\zeta,\xi)$ (see Appendix Appendix A) and N_ξ is an integer greater or equal to 1. Of course, in general, the exact solution to equation (16) does not have a finite Legendre spectrum, but taking N_ξ sufficiently high in expansion (29) yields an approximate solution to the desired degree of accuracy (in infinite precision arithmetic).

In Appendix Appendix A we derive explicitly the projection of each term of the drift-kinetic equation (16) onto the Legendre basis when the representation (29) is used. When doing so, we get that the Legendre modes of the drift-kinetic equation have the tridiagonal representation

$$L_k f^{(k-1)} + D_k f^{(k)} + U_k f^{(k+1)} = s^{(k)}, \tag{30}$$

for $k = 0, 1, \ldots, N_\xi$, where we have defined for convenience $f^{(-1)} := 0$ and from expansion (29) is clear that $f^{(N_\xi+1)} = 0$. Analogously to (29) the source term is expanded as $s = \sum_{k=0}^{N_\xi} s^{(k)}P_k$, and for the sources (17) this expansion is exact when $N_\xi \geq 2$. The spatial differential operators read

$$L_k = \frac{k}{2k-1}\left(\boldsymbol{b}\cdot\nabla + \frac{k-1}{2}\boldsymbol{b}\cdot\nabla\ln B\right), \tag{31}$$

$$D_k = -\frac{\hat{E}_\psi}{\langle B^2\rangle}\boldsymbol{B}\times\nabla\psi\cdot\nabla + \frac{k(k+1)}{2}\hat{\nu}, \tag{32}$$

$$U_k = \frac{k+1}{2k+3}\left(\boldsymbol{b}\cdot\nabla - \frac{k+2}{2}\boldsymbol{b}\cdot\nabla\ln B\right). \tag{33}$$

Thanks to its tridiagonal structure, the system of equations (30) can be formally inverted using the standard Gaussian elimination algorithm for block tridiagonal matrices. Before introducing the algorithm we will explain how to fix the free constant of the solution to equation (30) so that it can be inverted. Note that the aforementioned nullspace of the drift-kinetic equation translates in the fact that $f^{(0)}$ is not completely determined from equation (30). To prove this, we inspect the modes $k = 0$ and $k = 1$ that involve $f^{(0)}$. From expression (28) we can deduce that the term $D_0 f^{(0)} + U_0 f^{(1)}$ is invariant if we add to $f^{(0)}$ any function of $B_\theta(\psi)\zeta + B_\zeta(\psi)\theta$ when $\hat{E}_\psi \neq 0$ and does not include $f^{(0)}$ for $\hat{E}_\psi = 0$. Besides, the term $L_1 f^{(0)} + D_1 f^{(1)} + U_1 f^{(2)}$ remains invariant if

we add to $f^{(0)}$ any constant. Thus, equation (30) is unaltered when we add to $f^{(0)}$ a constant. A constraint equivalent to condition (11) is to fix the value of the $0-$th Legendre mode of the distribution function at a single point of the flux-surface. For example,

$$f^{(0)}(0,0) = 0. \tag{34}$$

With this condition, equation (30) has a unique solution and can be inverted (further details on its invertibility are given in Appendix Appendix B) to obtain an approximation of the first $N_\xi + 1$ Legendre modes of the solution to the drift-kinetic equation (16).

The algorithm for formally solving the truncated drift-kinetic equation (30) consists of two steps.

(i) **Forward elimination**

Starting from $\Delta_{N_\xi} = D_{N_\xi}$ and $\sigma^{(N_\xi)} = s^{(N_\xi)}$ we can obtain recursively the operators

$$\Delta_k = D_k - U_k \Delta_{k+1}^{-1} L_{k+1}, \tag{35}$$

and the sources

$$\sigma^{(k)} = s^{(k)} - U_k \Delta_{k+1}^{-1} \sigma^{(k+1)}, \tag{36}$$

for $k = N_\xi - 1, N_\xi - 2, \ldots, 0$ (in this order). Equations (35) and (36) define the forward elimination. With this procedure we can transform equation (30) to the equivalent system

$$L_k f^{(k-1)} + \Delta_k f^{(k)} = \sigma^{(k)}, \tag{37}$$

for $k = 0, 1, \ldots, N_\xi$. Note that this process corresponds to perform formal Gaussian elimination over

$$\left[\begin{array}{ccc|c} L_k & D_k & U_k & s^{(k)} \\ 0 & L_{k+1} & \Delta_{k+1} & \sigma^{(k+1)} \end{array}\right], \tag{38}$$

to eliminate U_k in the first row.

(ii) **Backward substitution**

Once we have the system of equations in the form (37) it is immediate to solve recursively

$$f^{(k)} = \Delta_k^{-1} \left(\sigma^{(k)} - L_k f^{(k-1)} \right), \tag{39}$$

for $k = 0, 1, ..., N_\xi$ (in this order). Here, we denote by $\Delta_0^{-1}\sigma^{(0)}$ to the solution that satisfies (34). We recall that for $k = 0$, we must impose condition (34) so that $\Delta_0 f^{(0)} = \sigma^{(0)}$ has a unique solution. As $L_1 = \boldsymbol{b} \cdot \nabla$, using expression (27), it is apparent from equation (39) that the integration constant does not affect the value of $f^{(1)}$.

We can apply this algorithm to solve equation (16) for f_1, f_2 and f_3 in order to compute approximations to the transport coefficients. In terms of the Legendre modes of f_1, f_2 and f_3, the monoenergetic geometric coefficients from definition (24) read

$$\widehat{D}_{11} = 2\left\langle s_1^{(0)} f_1^{(0)} \right\rangle + \frac{2}{5}\left\langle s_1^{(2)} f_1^{(2)} \right\rangle, \tag{40}$$

$$\widehat{D}_{31} = \frac{2}{3}\left\langle B f_1^{(1)} \right\rangle, \tag{41}$$

$$\widehat{D}_{13} = 2\left\langle s_1^{(0)} f_3^{(0)} \right\rangle + \frac{2}{5}\left\langle s_1^{(2)} f_3^{(2)} \right\rangle, \tag{42}$$

$$\widehat{D}_{33} = \frac{2}{3}\left\langle B f_3^{(1)} \right\rangle, \tag{43}$$

where $3s_1^{(0)}/2 = 3s_1^{(2)} = \boldsymbol{B} \times \nabla\psi \cdot \nabla B / B^3$. Note that, in order to compute the monoenergetic geometric coefficients $\widehat{D}_{ij}$ from expressions (40), (41), (42) and (43), we only need to calculate the Legendre modes $k = 0, 1, 2$ of the solution and we can stop the backward substitution (39) at $k = 2$. In the next subsection we will explain how `MONKES` approximately solves equation (30) using this algorithm.

3.2. Spatial discretization and algorithm implementation

The algorithm described above allows, in principle, to compute the exact solution to the truncated drift-kinetic equation (30) which is an approximate solution to (16). However, it is not possible, to our knowledge, to give an exact expression for the operator Δ_k^{-1} except for $k = N_\xi \geq 1$. Instead, we are forced to compute an approximate solution to (30). In order to obtain an approximate solution of equation (30) we assume that each $f^{(k)}$ has a finite Fourier spectrum so that it can be expressed as

$$f^{(k)}(\theta, \zeta) = \boldsymbol{I}(\theta, \zeta) \cdot \boldsymbol{f}^{(k)}, \tag{44}$$

where the Fourier interpolant row vector map $\boldsymbol{I}(\theta, \zeta)$ is defined at Appendix Appendix C and the column vector $\boldsymbol{f}^{(k)} \in \mathbb{R}^{N_{\text{fs}}}$ contains $f^{(k)}$ evaluated at the equispaced grid points

$$\theta_i = 2\pi i / N_\theta, \qquad i = 0, 1, \ldots, N_\theta - 1, \tag{45}$$

$$\zeta_j = 2\pi j / (N_\zeta N_p), \qquad j = 0, 1, \ldots, N_\zeta - 1. \tag{46}$$

Here, $N_{\text{fs}} := N_\theta N_\zeta$ is the number of points in which we discretize the flux surface being N_θ and N_ζ respectively the number of points in which we divide θ and ζ. The exact solution to equation (30) in general has an infinite Fourier spectrum and cannot exactly be written as (44), but taking N_θ and N_ζ sufficiently big, we can approximate the solution to equation (30) to arbitrary degree of accuracy (in infinite precision arithmetic). As is explained in Appendix Appendix C, introducing the Fourier interpolant (44) in equation (30) and then evaluating the result at the grid points, we obtain a system of $N_{\text{fs}} \times (N_\xi + 1)$ equations which can be solved

for $\{\boldsymbol{f}^{(k)}\}_{k=0}^{N_\xi}$. This system of equations is obtained by substituting the operators L_k, D_k, U_k in equation (30) by the $N_{\rm fs} \times N_{\rm fs}$ matrices $\boldsymbol{L}_k$, $\boldsymbol{D}_k$, $\boldsymbol{U}_k$, defined in Appendix Appendix C. Thus, we discretize (30) as

$$\boldsymbol{L}_k \boldsymbol{f}^{(k-1)} + \boldsymbol{D}_k \boldsymbol{f}^{(k)} + \boldsymbol{U}_k \boldsymbol{f}^{(k+1)} = \boldsymbol{s}^{(k)}, \tag{47}$$

for $k = 0, 1 \ldots, N_\xi$. Obviously, this system has a block tridiagonal structure and the algorithm presented in subsection 3.1 can be applied to it. We just have to replace in equations (35), (36) and (39) the operators and functions by their matrix and vector analogues respectively. We will denote such matrix and vector analogues by boldface letters. The matrix approximation to the forward elimination procedure given by equations (35) and (36) reads

$$\boldsymbol{\Delta}_k = \boldsymbol{D}_k - \boldsymbol{U}_k \boldsymbol{\Delta}_{k+1}^{-1} \boldsymbol{L}_{k+1}, \tag{48}$$

$$\boldsymbol{\sigma}^{(k)} = \boldsymbol{s}^{(k)} - \boldsymbol{U}_k \boldsymbol{\Delta}_{k+1}^{-1} \boldsymbol{\sigma}^{(k+1)}, \tag{49}$$

for $k = N_\xi - 1, N_\xi - 2, \ldots, 0$ (in this order). Thus, starting from $\boldsymbol{\Delta}_{N_\xi} = \boldsymbol{D}_{N_\xi}$ and $\boldsymbol{\sigma}^{(N_\xi)} = \boldsymbol{s}^{(N_\xi)}$ all the matrices $\boldsymbol{\Delta}_k$ and the vectors $\boldsymbol{\sigma}^{(k)}$ are defined from equations (48) and (49). Obtaining the matrix $\boldsymbol{\Delta}_k$ from equation (48) requires to invert $\boldsymbol{\Delta}_{k+1}$, perform two matrix multiplications and a subtraction of matrices. The inversion using LU factorization and each matrix multiplication require $O(N_{\rm fs}^3)$ operations so it is desirable to reduce the number of matrix multiplications to one. For $k \geq 2$, we can reduce the number of matrix multiplications in determining $\boldsymbol{\Delta}_k$ to one if instead of computing $\boldsymbol{\Delta}_{k+1}^{-1}$ we solve for $\boldsymbol{X}_{k+1}$ the matrix system of equations

$$\boldsymbol{\Delta}_{k+1} \boldsymbol{X}_{k+1} = \boldsymbol{L}_{k+1}, \tag{50}$$

and then obtain

$$\boldsymbol{\Delta}_k = \boldsymbol{D}_k - \boldsymbol{U}_k \boldsymbol{X}_{k+1}, \tag{51}$$

for $k = N_\xi - 1, N_\xi - 2, \ldots, 2$. For $k \leq 1$ as we need to solve (37) and do the backward substitution (39), it is convenient to compute and store $\boldsymbol{\Delta}_k^{-1}$. Besides, as none of the source terms s_1, s_2 and s_3 given by (17) have Legendre modes greater than 2 we have from equation (49) that $\boldsymbol{\sigma}^{(k)} = 0$ for $k \geq 3$ and $\boldsymbol{\sigma}^{(2)} = \boldsymbol{s}^{(2)}$ and (49) must be applied just when $k = 0$ and $k = 1$. Applying once (49) requires $O(N_{\rm fs}^2)$ operations and its contribution to the arithmetic complexity of the algorithm is subdominant with respect to the matrix inversions and multiplications. As the resolution of a matrix system of equations and matrix multiplication must be done $N_\xi + 1$ times, numerically solving equation (47) by this method requires $O(N_\xi N_{\rm fs}^3)$ operations.

In what concerns to memory resources, as we are only interested in the Legendre modes 0, 1 and 2, it is not necessary to store in memory all the matrices $\boldsymbol{L}_k$, $\boldsymbol{D}_k$, $\boldsymbol{U}_k$ and $\boldsymbol{\Delta}_k$. Instead, we store solely $\boldsymbol{L}_k$, $\boldsymbol{U}_k$ and $\boldsymbol{\Delta}_k^{-1}$ for $k = 0, 1, 2$. For the intermediate steps we just need to use some auxiliary matrices $\boldsymbol{L}$, $\boldsymbol{D}$, $\boldsymbol{U}$, $\boldsymbol{\Delta}$ and $\boldsymbol{X}$.

To summarize, the pseudocode of the implementation of the algorithm in `MONKES` is given in Algorithm 1. In the first loop from $k = N_\xi - 1$ to $k = 2$ we construct $\boldsymbol{L}_2$, $\boldsymbol{\Delta}_2^{-1}$ and $\boldsymbol{U}_2$ without saving any matrix from the intermediate steps nor computing any vector $\boldsymbol{\sigma}^{(k)}$. After that, in the second loop from $k = 1$ to $k = 0$, the matrices $\boldsymbol{L}_k$ and $\boldsymbol{\Delta}_k^{-1}$ are computed and saved for the posterior step of backward substitution.

Algorithm 1 Block tridiagonal solution algorithm implemented in `MONKES`.

Forward elimination:
- $\boldsymbol{L} \leftarrow \boldsymbol{L}_{N_\xi}$ ▷ Starting value for $\boldsymbol{L}$
- $\boldsymbol{\Delta} \leftarrow \boldsymbol{D}_{N_\xi}$ ▷ Starting value for $\boldsymbol{\Delta}$
- **for** $k = N_\xi - 1$ **to** 2 **do**
  - Solve $\boldsymbol{\Delta X} = \boldsymbol{L}$ ▷ Compute $\boldsymbol{X}_{k+1}$ stored in $\boldsymbol{X}$
  - $\boldsymbol{L} \leftarrow \boldsymbol{L}_k$ ▷ Construct $\boldsymbol{L}_k$ stored in $\boldsymbol{L}$
  - $\boldsymbol{D} \leftarrow \boldsymbol{D}_k$ ▷ Construct $\boldsymbol{D}_k$ stored in $\boldsymbol{D}$
  - $\boldsymbol{U} \leftarrow \boldsymbol{U}_k$ ▷ Construct $\boldsymbol{U}_k$ stored in $\boldsymbol{U}$
  - $\boldsymbol{\Delta} \leftarrow \boldsymbol{D} - \boldsymbol{UX}$ ▷ Construct $\boldsymbol{\Delta}_k$ stored in $\boldsymbol{\Delta}$
  - **if** $k = 2$ **then** ▷ Save required matrices
    - $\boldsymbol{L}_k \leftarrow \boldsymbol{L}$ ▷ Save $\boldsymbol{L}_2$
    - Solve $\boldsymbol{\Delta}\boldsymbol{\Delta}_k^{-1} = \text{Identity}$ ▷ Compute $\boldsymbol{\Delta}_2^{-1}$
    - $\boldsymbol{U}_k \leftarrow \boldsymbol{U}$ ▷ Save $\boldsymbol{U}_2$
  - **end if**
- **end for**
- **for** $k = 1$ to 0 **do**
  - **if** $k > 0$ $\boldsymbol{L}_k \leftarrow \boldsymbol{L}_k$ ▷ Construct and save $\boldsymbol{L}_k$
  - $\boldsymbol{D} \leftarrow \boldsymbol{D}_k$ ▷ Construct $\boldsymbol{D}_k$ stored in $\boldsymbol{D}$
  - $\boldsymbol{U}_k \leftarrow \boldsymbol{U}_k$ ▷ Construct and save $\boldsymbol{U}_k$
  - $\boldsymbol{\Delta}_k^{-1} \leftarrow \boldsymbol{D} - \boldsymbol{U}_k \boldsymbol{\Delta}_{k+1}^{-1} \boldsymbol{L}_k$ ▷ Construct $\boldsymbol{\Delta}_k$
  - $\boldsymbol{\sigma}^{(k)} \leftarrow \boldsymbol{s}^{(k)} - \boldsymbol{U}_k \boldsymbol{\Delta}_{k+1}^{-1} \boldsymbol{\sigma}^{(k+1)}$ ▷ Construct $\boldsymbol{\sigma}^{(k)}$
  - Solve $\boldsymbol{\Delta}\boldsymbol{\Delta}_k^{-1} = \text{Identity}$ ▷ Compute $\boldsymbol{\Delta}_k^{-1}$
- **end for**

Backward substitution:
- $\boldsymbol{f}^{(0)} \leftarrow \boldsymbol{\Delta}_0^{-1} \boldsymbol{\sigma}^{(0)}$
- **for** $k = 1$ **to** 2 **do**
  - $\boldsymbol{f}^{(k)} \leftarrow \boldsymbol{\Delta}_k^{-1} \left(\boldsymbol{\sigma}^{(k)} - \boldsymbol{L}_k \boldsymbol{f}^{(k-1)} \right)$
- **end for**

Once we have solved (47) for $\boldsymbol{f}^{(0)}$, $\boldsymbol{f}^{(1)}$ and $\boldsymbol{f}^{(2)}$, the integrals of the flux surface average operation involved in the geometric coefficients (40), (41), (42) and (43), are conveniently computed using the trapezoidal rule, which for periodic analytic functions has geometric convergence [36]. In the next sections we will see that despite the cubic scaling in $N_{\rm fs}$ of the arithmetical complexity of the algorithm, it is possible to obtain fast and accurate calculations

of the monoenergetic geometric coefficients at low collisionality (in particular $\widehat{D}_{31}$) in a single processor. The reason behind this is that in the asymptotic relation $O(N_{\rm fs}^3) \sim C_{\rm alg} N_{\rm fs}^3$, the constant $C_{\rm alg}$ is small enough to allow $N_{\rm fs}$ to take a value sufficiently high to capture accurately the spatial dependence of the distribution function without increasing much the wall-clock time. The algorithm is implemented in the new code `MONKES`, written in Fortran language. The matrix inversions and multiplications are computed using the linear algebra library `LAPACK` [37].

4. Numerical results and benchmark

4.1. Convergence of monoenergetic coefficients at low collisionality

4.2. Benchmark of monoenergetic coefficients

5. Conclusions and future work

Appendix A. Legendre modes of the drift-kinetic equation

Legendre polynomials are the eigenfunctions of the Sturm-Liouville problem in the interval $\xi \in [-1,1]$ defined by the differential equation

$$2\mathcal{L}P_k(\xi) = -k(k+1)P_k(\xi), \tag{A.1}$$

and regularity boundary conditions at $\xi = \pm 1$

$$(1-\xi^2)\frac{\mathrm{d}P_k}{\mathrm{d}\xi}\bigg|_{\xi=\pm 1} = 0, \tag{A.2}$$

where $k \geq 0$ is an integer.

As $\mathcal{L}$ has a discrete spectrum and is self-adjoint with respect to the inner product

$$\langle f, g\rangle_{\mathcal{L}} := \int_{-1}^{1} fg \,\mathrm{d}\xi\,, \tag{A.3}$$

in the space of functions that satisfy the regularity condition, $\{P_k\}_{k=0}^{\infty}$ is an orthogonal basis satisfying $\langle P_j, P_k\rangle_{\mathcal{L}} = 2\delta_{jk}/(2k+1)$. Hence, these polynomials satisfy the three-term recurrence formula

$$(2k+1)\xi P_k(\xi) = (k+1)P_{k+1}(\xi) + kP_{k-1}(\xi), \tag{A.4}$$

obtained by Gram-Schmidt orthogonalization, which starting from $P_0 = 1$ and $P_1 = \xi$ defines them all. Additionally, they satisfy the differential identity

$$(1-\xi^2)\frac{\mathrm{d}P_k}{\mathrm{d}\xi} = kP_{k-1}(\xi) - k\xi P_k(\xi). \tag{A.5}$$

Identities (A.4) and (A.5) are useful to represent tridiagonally the left-hand side of equation (16) when we use the expansion (29). The $k-$th Legendre mode of the term $\xi \boldsymbol{b}\cdot\nabla f$ is expressed in terms of the modes $f^{(k-1)}$ and $f^{(k+1)}$ using (A.4)

$$\langle \xi \boldsymbol{b}\cdot\nabla f, P_k\rangle_{\mathcal{L}} = \frac{2}{2k+1}\left[\frac{k}{2k-1}\,\boldsymbol{b}\cdot\nabla f^{(k-1)} + \frac{k+1}{2k+3}\,\boldsymbol{b}\cdot\nabla f^{(k+1)}\right]. \tag{A.6}$$

Combining both (A.4) and (A.5) allows to express the $k-$th Legendre mode of the mirror term $\nabla\cdot\boldsymbol{b}((1-\xi^2)/2)\,\partial f/\partial\xi$ in terms of the modes $f^{(k-1)}$ and $f^{(k+1)}$ as

$$\left\langle \frac{1}{2}(1-\xi^2)\nabla\cdot\boldsymbol{b}\frac{\partial f}{\partial \xi}, P_k\right\rangle_{\mathcal{L}} = \frac{\boldsymbol{b}\cdot\nabla\ln B}{2k+1}\left[\frac{k(k-1)}{2k-1}f^{(k-1)} - \frac{(k+1)(k+2)}{2k+3}f^{(k+1)}\right], \tag{A.7}$$

where we have also used $\nabla\cdot\boldsymbol{b} = -\boldsymbol{b}\cdot\nabla\ln B$. The term proportional to $\hat{E}_\psi$ is diagonal in a Legendre representation

$$\left\langle \frac{\hat{E}_\psi}{\langle B^2\rangle}\boldsymbol{B}\times\nabla\psi\cdot\nabla f, P_k\right\rangle_{\mathcal{L}} = \frac{2}{2k+1}\frac{\hat{E}_\psi}{\langle B^2\rangle}\boldsymbol{B}\times\nabla\psi\cdot\nabla f^{(k)}. \tag{A.8}$$

Finally, for the collision operator used in equation (16), as Legendre polynomials are eigenfunctions of the pitch-angle scattering operator, using (A.1) we obtain the diagonal representation

$$\langle \hat{\nu}\mathcal{L}f, P_k\rangle_{\mathcal{L}} = -\hat{\nu}\frac{k(k+1)}{2k+1}f^{(k)}. \tag{A.9}$$

Appendix B. Invertibility of the spatial differential operators

In this Appendix we will study the invertibility of the left-hand-side of (30). For this, we view L_k, D_k and U_k as operators from $\mathcal{F}$ to $\mathcal{F}$, where $\mathcal{F}$ is the space of smooth functions on the flux-surface equipped with the inner product

$$\langle f, g\rangle_{\mathcal{F}} = \frac{N_p}{4\pi^2}\oint\oint f\bar{g}\,\mathrm{d}\theta\,\mathrm{d}\zeta\,, \tag{B.1}$$

where $\bar{z}$ denotes the complex conjugate of z and the induced norm

$$\|f\|_{\mathcal{F}} := \sqrt{\langle f, f\rangle_{\mathcal{F}}}. \tag{B.2}$$

In this setting L_k, D_k and U_k are bounded operators from $\mathcal{F}$ to $\mathcal{F}$ as all the coefficients are smooth. The operators L_k and U_k given by (31) and (33) do not have a uniquely defined inverse as they have a non

zero kernel. This is a consequence of the fact that the parallel streaming operator

$$\mathcal{V}_{\parallel} = \xi \boldsymbol{b}\cdot\nabla + \nabla\cdot\boldsymbol{b}\frac{(1-\xi^2)}{2}\frac{\partial}{\partial\xi} \tag{B.3}$$

has a kernel consisting of functions $g((1-\xi^2)/B)$.

To study the invertibility of L_k and U_k we employ coordinates (α, l) where α is a poloidal angle that labels field lines and l is the magnetic field length. Note that we can study the invertibility of L_k and U_k by studying the existence of solutions to

$$\frac{\mathrm{d}h}{\mathrm{d}l} + a(\alpha,l)h = s(\alpha,l), \tag{B.4}$$

where $a(\alpha,l)$ and $s(\alpha,l)$ are smooth functions. It is easy to check that the general solution to (B.4) can be written as

$$h(\alpha,l) = (h_0(\alpha) + W(\alpha,l))\exp(-A(\alpha,l)), \tag{B.5}$$

where

$$A(\alpha,l) = \int_0^l a(\alpha,l')\,\mathrm{d}l', \tag{B.6}$$

and

$$W(\alpha,l) = \int_0^l s(\alpha,l')\exp(A(\alpha,l'))\,\mathrm{d}l' \tag{B.7}$$

satisfying $h(\alpha,0) = h_0(\alpha)$. Thus, the solution to (B.4) in the plane (α,l) is determined up to a constant $h_0(\alpha)$. Imposing continuity on the flux surface to solution (B.5) fixes under some circumstances for $a(\alpha,l)$, the constant h_0. When ι is rational the field line closes on itself after a length L, thus continuity imposes $h(\alpha, l+L) = h(\alpha,l)$. In particular, continuity at $l=0$ imposes

$$h_0(\alpha) = (h_0(\alpha) + W(\alpha,L))\exp(-A(\alpha,L)). \tag{B.8}$$

If $A(\alpha,L) \neq 0$, continuity condition (B.8) fixes the value of $h_0(\alpha)$ as

$$h_0(\alpha) = W(\alpha,L)\frac{\exp(-A(\alpha,L))}{1-\exp(-A(\alpha,L))} \tag{B.9}$$

An equivalent manner to fix h_0 comes from integrating (B.4) along the field line combined with (B.5). For rational surfaces we integrate in the interval $[0,L]$

$$A(\alpha,L)h_0(\alpha) = \int_0^L s\,\mathrm{d}l - \int_0^L a\exp(-A)W\,\mathrm{d}l \tag{B.10}$$

which also reveals that when $A(\alpha,L) \neq 0$ equation (B.4) fixes h on the torus completely.

For irrational flux surfaces, we take the limit $L\to\infty$ in condition (B.8) to obtain

$$h_0(\alpha) = h_0(\alpha)\lim_{L\to\infty}\exp(-A(\alpha,L)) + \lim_{L\to\infty} W(\alpha,L)\exp(-A(\alpha,L)). \tag{B.11}$$

Thus, the integration constant h_0 can be determined from (B.11) when $\lim_{L\to\infty} A(\alpha,L) \neq 0$ and the limit $\lim_{L\to\infty} W(\alpha,L)\exp(-A(\alpha,L))$ exists. When it is possible to fix h_0 in irrational surfaces, it is a flux function. A more convenient expression to fix h_0 comes from dividing equation (B.10) by $\int_0^L \mathrm{d}l\,/B$ and taking the limit $L\to\infty$ to obtain

$$\langle Ba\rangle h_0 = \langle Bs\rangle - \langle Ba\exp(-A)W\rangle. \tag{B.12}$$

Note that if L_k and U_k are written in the form of (B.4), for both operators, the correspondent function $a(\alpha,l)$ is proportional to $\partial\ln B/\partial l$. This means that for rational surfaces $A(\alpha,L) = 0$ and when ι is irrational $\lim_{L\to\infty} A(\alpha,L) = 0$ or equivalently $\langle Ba\rangle = 0$. Thus, in both cases, there are infinitely many smooth solutions to (B.4) which proves that L_k and U_k are not one-to-one. Equivalently, all functions of the form $h_0\exp(-A)$ (for the appropriate A) belong to the kernel of L_k and U_k. Moreover, we obtain conditions on the source $s(\alpha,l)$. For rational surfaces, $W(\alpha,L) = 0$ or equivalently $\int_0^L s\,\mathrm{d}l = \int_0^L a\exp(-A)W\,\mathrm{d}l$ and for irrational surfaces $\lim_{L\to\infty} W(\alpha,L) = 0$ or equivalently $\langle Bs\rangle = \langle Ba\exp(-A)W\rangle$. This means that if we choose a smooth function on the flux surface h and apply either L_k or U_k, the images $L_k h$ or $U_k h$ have to satisfy these extra conditions. This proves that L_k and U_k are not onto. Therefore, they are clearly not invertible.

Now we will prove that if $\hat{\nu} \neq 0$, all the D_k for $k \geq 1$ are invertible. For $\hat{E}_\psi = 0$, D_k is just a multiplication operator and is obviously invertible if $k \neq 0$. When $\hat{E}_\psi \neq 0$ the proof can be done using a similar argument to the one used for L_k and U_k, as we can transform D_k to an equation superficially very similar to (B.4). First, we change from Boozer angles (ψ,θ,ζ) to a different set of magnetic coordinates $(\tilde{\psi},\alpha,\varphi)$ using the linear transformation

$$\begin{bmatrix}\psi\\ \theta\\ \zeta\end{bmatrix} = \begin{bmatrix}1 & 0 & 0\\ 0 & (1+\iota\delta)^{-1} & \iota\\ 0 & -\delta(1+\iota\delta)^{-1} & 1\end{bmatrix}\begin{bmatrix}\tilde{\psi}\\ \alpha\\ \varphi\end{bmatrix} \tag{B.13}$$

where $\delta = B_\theta/B_\zeta$. In these coordinates $\boldsymbol{B} = \nabla\tilde{\psi}\times\nabla\alpha = B_{\tilde{\psi}}\nabla\tilde{\psi} + B_\varphi\nabla\varphi$ and

$$\boldsymbol{B}\times\nabla\tilde{\psi}\cdot\nabla = B^2\frac{\partial}{\partial\alpha}. \tag{B.14}$$

Thus, in coordinates (α, φ), the operator D_k takes the form

$$D_k = -\hat{E}_\psi \frac{B^2}{\langle B^2 \rangle} \frac{\partial}{\partial \alpha} + \hat{\nu} \frac{k(k+1)}{2}. \tag{B.15}$$

Hence, we want to prove that

$$-\hat{E}_\psi \frac{B^2}{\langle B^2 \rangle} \frac{\partial g}{\partial \alpha} + \hat{\nu} \frac{k(k+1)}{2} g = s(\alpha, \varphi) \tag{B.16}$$

has a unique smooth solution for any source s. The general solution to this equation is

$$g = (g_0(\varphi) + K(\alpha, \varphi)) \exp(A_k(\alpha, \varphi)), \tag{B.17}$$

where $g_0(\varphi)$ is an integration constant,

$$K(\alpha, \varphi) = -\frac{\langle B^2 \rangle}{E_\psi} \times \int_0^\alpha s(\alpha', \varphi) \exp(-A_k(\alpha', \varphi)) \frac{\mathrm{d}\alpha'}{B^2(\alpha', \varphi)} \tag{B.18}$$

and

$$A_k(\alpha, \varphi) = \hat{\nu} \frac{k(k+1)}{2} \frac{\langle B^2 \rangle}{\hat{E}_\psi} \int_0^\alpha \frac{\mathrm{d}\alpha''}{B^2(\alpha'', \varphi)}. \tag{B.19}$$

Note from (B.13), that the curves of constant φ are straight lines in the (θ, ζ) plane with slope $-\delta$. This means that there are two options if we follow one of these curves: if $\delta \in \mathbb{Q}$ it closes on itself or if $\delta \in \mathbb{R} \backslash \mathbb{Q}$ it densely fills the whole flux surface. Applying the same continuity argument used for (B.5) we obtain that in order to fix g_0 either

$$A_k(L_\alpha, \varphi) \neq 0, \quad \text{if } \delta \in \mathbb{Q}, \tag{B.20}$$

or

$$\lim_{\alpha \to \infty} A_k(\alpha, \varphi) \neq 0, \quad \text{if } \delta \in \mathbb{R} \backslash \mathbb{Q}, \tag{B.21}$$

where $L_\alpha > 0$ is the arc-length required for the curve of constant φ to close on itself. However, with the exception of A_0 which is identically zero, A_k is monotonically crescent with α. For $k \geq 1$ we can write the integration constant as

$$g_0(\varphi) = -\frac{K(L_\alpha, \varphi)}{1 - \exp(-A_k(L_\alpha, \varphi))}, \qquad \text{if } \delta \in \mathbb{Q}, \tag{B.22}$$

or

$$g_0 = -\lim_{\alpha \to \infty} K(\alpha, \varphi), \qquad \text{if } \delta \in \mathbb{R} \backslash \mathbb{Q}. \tag{B.23}$$

Similarly to the constant h_0, we can obtain equivalent expressions by integrating the differential equation. When $\delta \in \mathbb{Q}$ applying $\int_0^{L_\alpha} \text{Eq. (B.16)} \, \mathrm{d}\alpha \, / B^2$ combined with (B.17) gives

$$g_0(\varphi) = \frac{2}{k(k+1)\hat{\nu}} \frac{\int_0^{L_\alpha} s \, \mathrm{d}\alpha \, / B^2}{\int_0^{L_\alpha} \exp(A_k) \, \mathrm{d}\alpha \, / B^2} - \frac{\int_0^{L_\alpha} K \exp(A_k) \, \mathrm{d}\alpha \, / B^2}{\int_0^{L_\alpha} \exp(A_k) \, \mathrm{d}\alpha \, / B^2} \tag{B.24}$$

Note that the annihilator for $\boldsymbol{B} \times \nabla \tilde{\psi} \cdot \nabla$ is the flux surface average, i.e. $\left\langle \boldsymbol{B} \times \nabla \tilde{\psi} \cdot \nabla f \right\rangle = 0$ for any univaluated function on the torus. Using this we can get a more explicit expression for g_0 when $\delta \in \mathbb{R} \backslash \mathbb{Q}$. Taking the flux surface average of (B.16) combined with (B.17) gives

$$g_0 = \frac{2}{k(k+1)\hat{\nu}} \frac{\langle s \rangle}{\langle \exp(A_k) \rangle} - \frac{\langle K \exp(A_k) \rangle}{\langle \exp(A_k) \rangle}. \tag{B.25}$$

Hence, for $k \geq 1$, we can write the inverse of D_k as the linear operator

$$D_k^{-1} s = (g_0(\varphi) + K(\alpha, \varphi)) \exp(A_k(\alpha, \varphi)),$$

where g_0 is given by (B.24) or (B.25) and is straightforward to check that $D_k D_k^{-1} s = D_k^{-1} D_k s = s$. The operator D_0 is not invertible as it is identically zero for $\hat{E}_\psi = 0$ and $A_0 = 0$ for $\hat{E}_\psi \neq 0$.

Finally, we will study the invertibility of the operator Δ_k

$$\Delta_k = D_k - U_k \Delta_{k+1}^{-1} L_{k+1} \tag{B.26}$$

assuming that Δ_{k+1} is bounded and invertible. For this, first, we note that in the space of functions of interest (smooth periodic functions on the torus), using a Fourier basis $\{e^{\mathrm{i}(m\theta + nN_p\zeta)}\}_{m,n \in \mathbb{Z}}$, we can approximate any function $f(\theta, \zeta) = \sum_{m,n \in \mathbb{Z}} \hat{f}_{mn} e^{\mathrm{i}(m\theta + nN_p\zeta)} \in \mathcal{F}$ using an approximant $\tilde{f}(\theta, \zeta)$

$$\tilde{f}(\theta, \zeta) = \sum_{-N \leq m,n \leq N} \hat{f}_{mn} e^{\mathrm{i}(m\theta + nN_p\zeta)} \tag{B.27}$$

truncating the modes with mode number greater than some positive integer N where

$$\hat{f}_{mn} = \left\langle f, e^{\mathrm{i}(m\theta + nN_p\zeta)} \right\rangle_{\mathcal{F}} \left\| e^{\mathrm{i}(m\theta + nN_p\zeta)} \right\|_{\mathcal{F}}^{-2} \tag{B.28}$$

are the Fourier modes of f. Thus, we approximate $\mathcal{F}$ using a finite dimensional subspace $\mathcal{F}^N \subset \mathcal{F}$ consisting on all the functions of the form given by equation (B.27).

Hence, as they are bounded operators, we can approximate D_k, U_k, Δ_{k+1} and L_{k+1} restricted to $\mathcal{F}^N$ (and therefore Δ_k) in equation (B.26) by operators D_k^N, U_k^N, Δ_{k+1}^N and L_{k+1}^N that map any $\tilde{f} \in \mathcal{F}^N$ to the projections of $D_k \tilde{f}$, $U_k \tilde{f}$, $\Delta_{k+1} \tilde{f}$ and $L_{k+1} \tilde{f}$ onto $\mathcal{F}^N$.

The operators D_k^N, U_k^N, Δ_{k+1}^N and L_{k+1}^N can be exactly represented (in a Fourier basis) by square matrices of size $\dim \mathcal{F}^N$. When the operators are invertible, these matrices are invertible aswell. Doing so, we can interpret the matrix representation of Δ_k as the Schur complement of the matrix

$$M_k^N = \begin{bmatrix} D_k^N & U_k^N \\ L_{k+1}^N & \Delta_{k+1}^N \end{bmatrix}. \tag{B.29}$$

It is well known from linear algebra that the Schur complement of M_k^N is invertible when both D_k^N and Δ_{k+1}^N are (which they are). Hence, for $k \geq 1$, the matrix representation of Δ_k^N can be inverted for any N, and therefore Δ_k is invertible. For $k = 0$, it is necessary to substitute one of the rows of $[D_k^N \quad U_k^N]$ by the condition (34) so that M_k^N is invertible for any N and as Δ_1^N can be inverted, also Δ_0^N constructed in this manner for any N, which implies that Δ_0 is invertible.

Appendix C. Fourier collocation method

In this appendix we describe the Fourier collocation (also called pseudospectral) method for discretizing the angles θ and ζ. This discretization will be used to obtain the matrices $\boldsymbol{L}_k$, $\boldsymbol{D}_k$ and $\boldsymbol{U}_k$. For convenience, we will use the complex version of the discretization method but for the discretization matrices we will just take their real part as the solutions to (16) are all real. We search for approximate solutions to equation (30) of the form

$$f^{(k)}(\theta,\zeta) = \sum_{n=-N_{\zeta 1}/2}^{N_{\zeta 2}/2-1} \sum_{m=-N_{\theta 1}/2}^{N_{\theta 2}/2-1} \tilde{f}_{mn}^{(k)} e^{\mathrm{i}(m\theta + nN_p\zeta)} \tag{C.1}$$

where $N_{\theta 1} = N_\theta - N_\theta \mod 2$, $N_{\theta 2} = N_\theta + N_\theta \mod 2$, $N_{\zeta 1} = N_\zeta - N_\zeta \mod 2$, $N_{\zeta 2} = N_\zeta + N_\zeta \mod 2$ for some positive integers N_θ, N_ζ. The complex numbers

$$\tilde{f}_{mn}^{(k)} := \left\langle f^{(k)}, e^{\mathrm{i}(m\theta+nN_p\zeta)} \right\rangle_{N_\theta N_\zeta} \left\| e^{\mathrm{i}(m\theta+nN_p\zeta)} \right\|_{N_\theta N_\zeta}^{-2} \tag{C.2}$$

are the discrete Fourier modes (also called discrete Fourier transform),

$$\langle f, g \rangle_{N_\theta N_\zeta} := \frac{1}{N_\theta N_\zeta} \sum_{j'=0}^{N_\zeta-1} \sum_{i'=0}^{N_\theta-1} f(\theta_{i'}, \zeta_{j'}) \overline{g(\theta_{i'}, \zeta_{j'})}, \tag{C.3}$$

is the discrete inner product associated to the equispaced grid points (45), (46), $\|f\|_{N_\theta N_\zeta} := \sqrt{\langle f, f \rangle_{N_\theta N_\zeta}}$ its induced norm and $\bar{z}$ denotes the complex conjugate of z. We denote by $\mathcal{F}^{N_\theta N_\zeta}$ to the finite dimensional vector space (of dimension $N_\theta N_\zeta$) comprising all the functions that can be written in the form of expansion (C.1).

The set of functions $\{e^{\mathrm{i}(m\theta+nN_p\zeta)}\} \subset \mathcal{F}^{N_\theta N_\zeta}$ forms an orthogonal basis for $\mathcal{F}^{N_\theta N_\zeta}$ equipped with the discrete inner product (C.3). Namely,

$$\left\langle e^{\mathrm{i}(m\theta+nN_p\zeta)}, e^{\mathrm{i}(m'\theta+n'N_p\zeta)} \right\rangle_{N_\theta N_\zeta} \propto \delta_{mm'}\delta_{nn'} \tag{C.4}$$

for $-N_{\theta 1}/2 \leq m \leq N_{\theta 2}/2$ and $-N_{\zeta 1}/2 \leq n \leq N_{\zeta 2}/2$. Thus, for functions lying in $\mathcal{F}^{N_\theta N_\zeta}$, discrete expansions such as (C.1) coincide with their (finite) Fourier series. The discrete Fourier modes (C.2) are chosen so that the expansion (C.1) interpolates $f^{(k)}$ at grid points. Thus, there is a vector space isomorphism between the space of discrete Fourier modes and $f^{(k)}$ evaluated at the equispaced grid.

Combining equations (C.1), (C.2) and (C.3) we can write our Fourier interpolant as

$$\begin{aligned} f^{(k)}(\theta,\zeta) &= \boldsymbol{I}(\theta,\zeta) \cdot \boldsymbol{f}^{(k)} \\ &= \sum_{j'=0}^{N_\zeta-1} \sum_{i'=0}^{N_\theta-1} I_{i'j'}(\theta,\zeta) f^{(k)}(\theta_{i'}, \zeta_{j'}), \end{aligned} \tag{C.5}$$

where $\boldsymbol{f}^{(k)} \in \mathbb{R}^{N_{\mathrm{fs}}}$ is the state vector containing $f^{(k)}(\theta_{i'}, \zeta_{j'})$. The entries of the vector $\boldsymbol{I}(\theta,\zeta)$ are the functions $I_{i'j'}(\theta,\zeta)$ given by,

$$I_{i'j'}(\theta,\zeta) = I_{i'}^\theta(\theta) I_{j'}^\zeta(\zeta), \tag{C.6}$$

$$I_{i'}^\theta(\theta) = \frac{1}{N_\theta} \sum_{m=-N_{\theta 1}/2}^{N_{\theta 2}/2-1} e^{\mathrm{i}m(\theta-\theta_{i'})}, \tag{C.7}$$

$$I_{j'}^\zeta(\zeta) = \frac{1}{N_\zeta} \sum_{n=-N_{\zeta 1}/2}^{N_{\zeta 2}/2-1} e^{N_p \mathrm{i}n(\zeta-\zeta_{j'})}. \tag{C.8}$$

Note that the interpolant is the only function in $\mathcal{F}^{N_\theta N_\zeta}$ which interpolates the data at the grid points, as $I_{i'}^\theta(\theta_i) = \delta_{ii'}$ and $I_{j'}^\zeta(\zeta_j) = \delta_{jj'}$.

Of course, our approximation (C.5) cannot (in general) be a solution to (30) at all points $(\theta,\zeta) \in [0, 2\pi) \times [0, 2\pi/N_p)$. Instead, we will force that the interpolant (C.5) solves equation (30) exactly at the equispaced grid points. Thanks to the vector space isomorphism (C.2) between $\boldsymbol{f}^{(k)}$ and the discrete modes $\tilde{f}_{mn}^{(k)}$ this is equivalent to match the discrete Fourier modes of the left and right-hand-sides of equation (30).

Inserting the interpolant (C.5) in the left-hand side of equation (30) and evaluating the result at grid

points gives

$$\left(L_k f^{(k-1)} + D_k f^{(k)} + U_k f^{(k)}\right)\Big|_{(\theta_i,\zeta_j)} = \left(L_k \boldsymbol{I}\cdot\boldsymbol{f}^{(k-1)} + D_k \boldsymbol{I}\cdot\boldsymbol{f}^{(k)} + U_k \boldsymbol{I}\cdot\boldsymbol{f}^{(k+1)}\right)\Big|_{(\theta_i,\zeta_j)}. \tag{C.9}$$

Here, $L_k\boldsymbol{I}(\theta_i,\zeta_j)$, $D_k\boldsymbol{I}(\theta_i,\zeta_j)$ and $U_k\boldsymbol{I}(\theta_i,\zeta_j)$ are respectively the rows of $\boldsymbol{L}_k$, $\boldsymbol{D}_k$ and $\boldsymbol{U}_k$ associated to the grid point (θ_i,ζ_j). We can relate them to the actual positions they will occupy in the matrices choosing an ordenation of rows and columns. If we use the ordenation that relates respectively the row i_r and column i_c to the grid points (θ_i,ζ_j) and $(\theta_{i'},\zeta_{j'})$ as

$$i_\mathrm{r} = 1 + i + jN_\theta, \tag{C.10}$$
$$i_\mathrm{c} = 1 + i' + j'N_\theta, \tag{C.11}$$

for $i,i' = 0,1,\ldots,N_\theta-1$ and $j,j' = 0,1,\ldots,N_\zeta-1$. With this ordenation, we define the elements of the row i_r and column i_c given by (C.10) and (C.11) of the matrices $\boldsymbol{L}_k$, $\boldsymbol{D}_k$ and $\boldsymbol{U}_k$ to be

$$(\boldsymbol{L}_k)_{i_\mathrm{r}i_\mathrm{c}} = L_k I_{i'j'}(\theta_i,\zeta_j), \tag{C.12}$$
$$(\boldsymbol{D}_k)_{i_\mathrm{r}i_\mathrm{c}} = D_k I_{i'j'}(\theta_i,\zeta_j), \tag{C.13}$$
$$(\boldsymbol{U}_k)_{i_\mathrm{r}i_\mathrm{c}} = U_k I_{i'j'}(\theta_i,\zeta_j). \tag{C.14}$$

Explicitly,

$$L_k I_{i'j'}\Big|_{(\theta_i,\zeta_j)} = \frac{k}{2k-1}\left(\boldsymbol{b}\cdot\nabla I_{i'j'}\Big|_{(\theta_i,\zeta_j)} + \frac{k-1}{2}\,\boldsymbol{b}\cdot\nabla\ln B\Big|_{(\theta_i,\zeta_j)}\delta_{ii'}\delta_{jj'}\right), \tag{C.15}$$

$$D_k I_{i'j'}\Big|_{(\theta_i,\zeta_j)} = \frac{\hat{E}_\psi}{\langle B^2\rangle}\,\boldsymbol{B}\times\nabla\psi\cdot\nabla I_{i'j'}\Big|_{(\theta_i,\zeta_j)} + \frac{k(k+1)}{2}\hat{\nu}\delta_{ii'}\delta_{jj'}, \tag{C.16}$$

$$U_k I_{i'j'}\Big|_{(\theta_i,\zeta_j)} = \frac{k+1}{2k+3}\left(\boldsymbol{b}\cdot\nabla I_{i'j'}\Big|_{(\theta_i,\zeta_j)} + \frac{k+2}{2}\,\boldsymbol{b}\cdot\nabla\ln B\Big|_{(\theta_i,\zeta_j)}\delta_{ii'}\delta_{jj'}\right), \tag{C.17}$$

where we have used expressions (27) and (28) to write

$$\boldsymbol{b}\cdot\nabla I_{i'j'}\Big|_{(\theta_i,\zeta_j)} = \frac{B}{B_\zeta+\iota B_\theta}\Big|_{(\theta_i,\zeta_j)} \times\left(\iota\delta_{jj'}\,\frac{\mathrm{d}I^\theta_{i'}}{\mathrm{d}\theta}\Big|_{\theta_i} - \delta_{ii'}\,\frac{\mathrm{d}I^\zeta_{j'}}{\mathrm{d}\zeta}\Big|_{\zeta_j}\right) \tag{C.18}$$

$$\boldsymbol{B}\times\nabla\psi\cdot\nabla I_{i'j'}\Big|_{(\theta_i,\zeta_j)} = \frac{B^2}{B_\zeta+\iota B_\theta}\Big|_{(\theta_i,\zeta_j)} \times\left(B_\zeta\delta_{jj'}\,\frac{\mathrm{d}I^\theta_{i'}}{\mathrm{d}\theta}\Big|_{\theta_i} - B_\theta\delta_{ii'}\,\frac{\mathrm{d}I^\zeta_{j'}}{\mathrm{d}\zeta}\Big|_{\zeta_j}\right) \tag{C.19}$$

We remark in first place that, for $k=0$, the rows of $\boldsymbol{D}_0$ and $\boldsymbol{U}_0$ associated to the grid point $(\theta_0,\zeta_0) = (0,0)$, are replaced by equation (34). Finally, each state vector $\boldsymbol{f}^{(k)}$ for the Fourier interpolants contains the images $f^{(k)}(\theta_{i'},\zeta_{j'})$ at the grid points, ordered according to (C.11).

Appendix D. Convergence of monoenergetic coefficients calculated by `DKES`

The code `DKES` gives an approximation to the monoenergetic geometric coefficients as a semisum of two quantities $\widehat{D}^-_{ij}$ and $\widehat{D}^+_{ij}$§ by solving a variational principle [31]. For each coefficient, the output of `DKES` consists on two columns containing $\widehat{D}^\mp_{ij}K_{ij}$, where K_{ij} are the normalization factors

$$K_{ij} := \left(\frac{\mathrm{d}\psi}{\mathrm{d}r}\right)^{-2}, \qquad i,j\in\{1,2\}, \tag{D.1}$$

$$K_{i3} := -\left(\frac{\mathrm{d}\psi}{\mathrm{d}r}B_{00}\right)^{-1}, \qquad i\in\{1,2\}, \tag{D.2}$$

$$K_{3j} := \left(\frac{\mathrm{d}\psi}{\mathrm{d}r}B_{00}\right)^{-1}, \qquad j\in\{1,2\}, \tag{D.3}$$

$$K_{33} := -B_{00}^{-2}, \tag{D.4}$$

where $B_{00} = N_p(2\pi)^{-2}\oint\oint B\,\mathrm{d}\theta\,\mathrm{d}\zeta$ is the $(0,0)$ Fourier mode of B.

In this Appendix we plot how the monoenergetic coefficients calculated by `DKES` converge. From the output of `DKES`, the two columns $\widehat{D}^\pm_{ij}$ satisfy $\widehat{D}^-_{ij}\geq\widehat{D}^+_{ij}$ and allow to compute bounds for $\widehat{D}_{ij}$

$$\frac{\widehat{D}^-_{ij}+\widehat{D}^+_{ij}}{2} - \Delta_{ij} \leq \widehat{D}_{ij} \leq \frac{\widehat{D}^-_{ij}+\widehat{D}^+_{ij}}{2} + \Delta_{ij} \tag{D.5}$$

and $\Delta_{ij} = \frac{1}{2}\sqrt{(\widehat{D}^-_{ii}-\widehat{D}^+_{ii})(\widehat{D}^-_{jj}-\widehat{D}^+_{jj})}$.

§ The columns

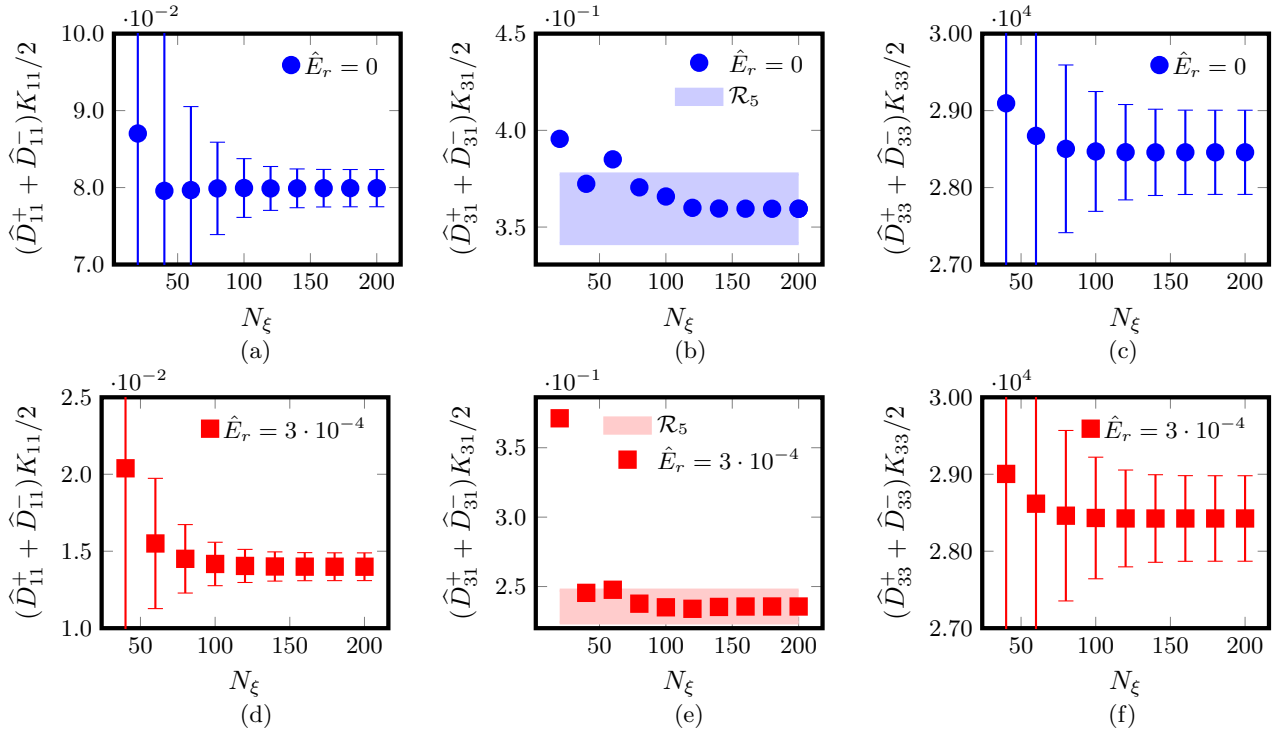

Figure D1: Convergence of monoenergetic coefficients calculated with `DKES` for W7X-EIM at the surface labelled by $\psi/\psi_{\mathrm{lcfs}} = 0.200$. $\hat{E}_r$ in $\mathrm{kV} \cdot \mathrm{s/m^2}$.

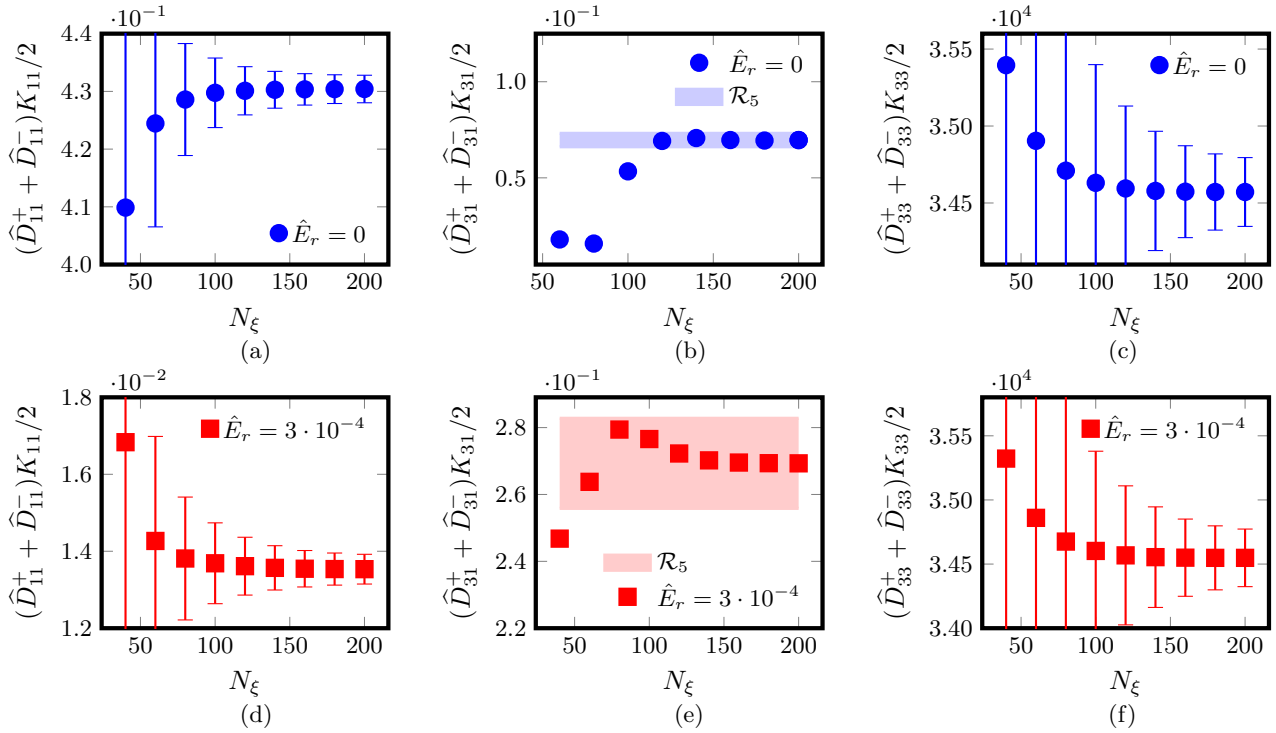

Figure D2: Convergence of monoenergetic coefficients calculated with `DKES` for W7X-KJM at the surface labelled by $\psi/\psi_{\mathrm{lcfs}} = 0.204$. $\hat{E}_r$ in $\mathrm{kV} \cdot \mathrm{s/m^2}$.

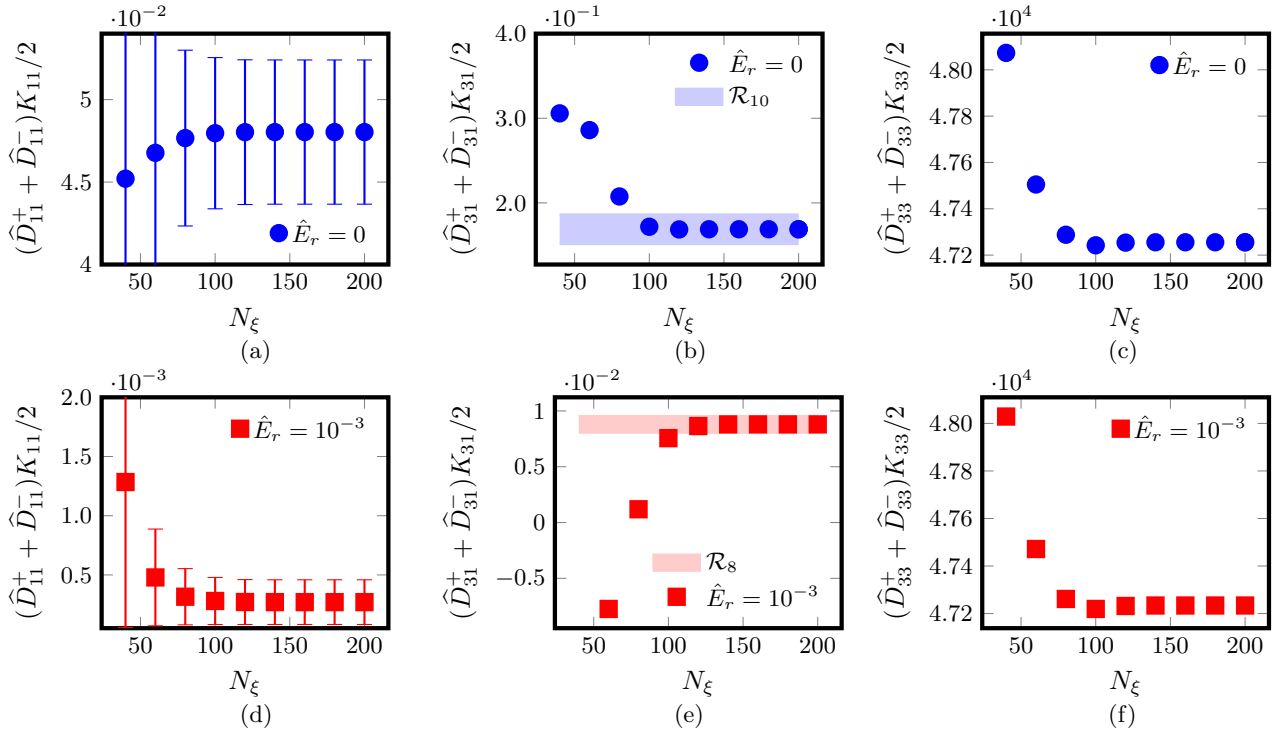

Figure D3: Convergence of monoenergetic coefficients calculated with `DKES` for CIEMAT-QI at the surface labelled by $\psi/\psi_{\mathrm{lcfs}} = 0.250$. $\hat{E}_r$ in $\mathrm{kV} \cdot \mathrm{s/m^2}$.

Acknowledgements

References

[1] Per Helander. Theory of plasma confinement in non-axisymmetric magnetic fields. *Reports on Progress in Physics*, 77(8):087001, jul 2014.

[2] C.D. Beidler, K. Allmaier, M.Yu. Isaev, S.V. Kasilov, W. Kernbichler, G.O. Leitold, H. Maaßberg, D.R. Mikkelsen, S. Murakami, M. Schmidt, D.A. Spong, V. Tribaldos, and A. Wakasa. Benchmarking of the mono-energetic transport coefficients—results from the international collaboration on neoclassical transport in stellarators (icnts). *Nuclear Fusion*, 51(7):076001, jun 2011.

[3] Iván Calvo, Felix I Parra, José Luis Velasco, and J Arturo Alonso. The effect of tangential drifts on neoclassical transport in stellarators close to omnigeneity. *Plasma Physics and Controlled Fusion*, 59(5):055014, mar 2017.

[4] Vincent d'Herbemont, Felix I. Parra, Iván Calvo, and José Luis Velasco. Finite orbit width effects in large aspect ratio stellarators. *Journal of Plasma Physics*, 88(5):905880507, 2022.

[5] John R. Cary and Svetlana G. Shasharina. Omnigenity and quasihelicity in helical plasma confinement systems. *Physics of Plasmas*, 4:3323–3333, 1997.

[6] P Helander and J Nührenberg. Bootstrap current and neoclassical transport in quasi-isodynamic stellarators. *Plasma Physics and Controlled Fusion*, 51(5):055004, feb 2009.

[7] P. Helander, J. Geiger, and H. Maaßberg. On the bootstrap current in stellarators and tokamaks. *Physics of Plasmas*, 18(9), 09 2011. 092505.

[8] C. D. Beidler, H. M. Smith, A. Alonso, T. Andreeva, J. Baldzuhn, M. N. A. Beurskens, M. Borchardt, S. A. Bozhenkov, K. J. Brunner, H. Damm, M. Drevlak, O. P. Ford, G. Fuchert, J. Geiger, P. Helander, U. Hergenhahn, M. Hirsch, U. Höfel, Ye. O. Kazakov, R. Kleiber, M. Krychowiak, S. Kwak, A. Langenberg, H. P. Laqua, U. Neuner, N. A. Pablant, E. Pasch, A. Pavone, T. S. Pedersen, K. Rahbarnia, J. Schilling, E. R. Scott, T. Stange, J. Svensson, H. Thomsen, Y. Turkin, F. Warmer, R. C. Wolf, D. Zhang, I. Abramovic, S. Äkäslompolo, J. Alcusón, P. Aleynikov, K. Aleynikova, A. Ali, G. Anda, E. Ascasibar, J. P. Bähner, S. G. Baek, M. Balden, M. Banduch, T. Barbui, W. Behr, A. Benndorf, C. Biedermann, W. Biel, B. Blackwell, E. Blanco, M. Blatzheim, S. Ballinger, T. Bluhm, D. Böckenhoff, B. Böswirth, L.-G. Böttger, V. Borsuk, J. Boscary, H.-S. Bosch, R. Brakel, H. Brand, C. Brandt, T. Bräuer, H. Braune, S. Brezinsek, K.-J. Brunner, R. Burhenn, R. Bussiahn, B. Buttenschön, V. Bykov, J. Cai, I. Calvo, B. Cannas, A. Cappa, A. Carls, L. Carraro, B. Carvalho, F. Castejon, A. Charl, N. Chaudhary, D. Chauvin, F. Chernyshev, M. Cianciosa, R. Citarella, G. Claps, J. Coenen, M. Cole, M. J. Cole, F. Cordella, G. Cseh, A. Czarnecka, K. Czerski, M. Czerwinski, G. Czymek, A. da Molin, A. da Silva, A. de la Pena, S. Degenkolbe, C. P. Dhard, M. Dibon, A. Dinklage, T. Dittmar, P. Drewelow, P. Drews, F. Durodie, E. Edlund, F. Effenberg, G. Ehrke, S. Elgeti, M. Endler, D. Ennis, H. Esteban, T. Estrada, J. Fellinger, Y. Feng, E. Flom, H. Fernandes, W. H. Fietz, W. Figacz, J. Fontdecaba, T. Fornal, H. Frerichs, A. Freund, T. Funaba, A. Galkowski, G. Gantenbein, Y. Gao, J. García Regaña, D. Gates, B. Geiger, V. Giannella, A. Gogoleva, B. Goncalves, A. Goriaev, D. Gradic, M. Grahl, J. Green, H. Greuner, A. Grosman, H. Grote, M. Gruca, O. Grulke, C. Guerard, P. Hacker, X. Han, J. H. Harris, D. Hartmann, D. Hathiramani, B. Hein,

B. Heinemann, S. Henneberg, M. Henkel, J. Hernandez Sanchez, C. Hidalgo, K. P. Hollfeld, A. Hölting, D. Höschen, M. Houry, J. Howard, X. Huang, Z. Huang, M. Hubeny, M. Huber, H. Hunger, K. Ida, T. Ilkei, S. Illy, B. Israeli, S. Jablonski, M. Jakubowski, J. Jelonnek, H. Jenzsch, T. Jesche, M. Jia, P. Junghanns, J. Kacmarczyk, J.-P. Kallmeyer, U. Kamionka, H. Kasahara, W. Kasparek, N. Kenmochi, C. Killer, A. Kirschner, T. Klinger, J. Knauer, M. Knaup, A. Knieps, T. Kobarg, G. Kocsis, F. Köchl, Y. Kolesnichenko, A. Könies, R. König, P. Kornejew, J.-P. Koschinsky, F. Köster, M. Krämer, R. Krampitz, A. Krämer-Flecken, N. Krawczyk, T. Kremeyer, J. Krom, I. Ksiazek, M. Kubkowska, G. Kühner, T. Kurki-Suonio, P. A. Kurz, M. Landreman, P. Lang, R. Lang, S. Langish, H. Laqua, R. Laube, S. Lazerson, C. Lechte, M. Lennartz, W. Leonhardt, C. Li, Y. Li, Y. Liang, C. Linsmeier, S. Liu, J.-F. Lobsien, D. Loesser, J. Loizu Cisquella, J. Lore, A. Lorenz, M. Losert, A. Lücke, A. Lumsdaine, V. Lutsenko, H. Maaßberg, O. Marchuk, J. H. Matthew, S. Marsen, M. Marushchenko, S. Masuzaki, D. Maurer, M. Mayer, K. McCarthy, P. McNeely, A. Meier, D. Mellein, B. Mendelevitch, P. Mertens, D. Mikkelsen, A. Mishchenko, B. Missal, J. Mittelstaedt, T. Mizuuchi, A. Mollen, V. Moncada, T. Mönnich, T. Morisaki, D. Moseev, S. Murakami, G. Náfrádi, M. Nagel, D. Naujoks, H. Neilson, R. Neu, O. Neubauer, T. Ngo, D. Nicolai, S. K. Nielsen, H. Niemann, T. Nishizawa, R. Nocentini, C. Nührenberg, J. Nührenberg, S. Obermayer, G. Offermanns, K. Ogawa, J. Ölmanns, J. Ongena, J. W. Oosterbeek, G. Orozco, M. Otte, L. Pacios Rodriguez, N. Panadero, N. Panadero Alvarez, D. Papenfuß, S. Paqay, E. Pawelec, G. Pelka, V. Perseo, and the W7-X Team. Demonstration of reduced neoclassical energy transport in wendelstein 7-x. *Nature*, 596(7871):221–226, Aug 2021.

[9] A. Dinklage, C. D. Beidler, P. Helander, G. Fuchert, H. Maaßberg, K. Rahbarnia, T. Sunn Pedersen, Y. Turkin, R. C. Wolf, A. Alonso, T. Andreeva, B. Blackwell, S. Bozhenkov, B. Buttenschön, A. Czarnecka, F. Effenberg, Y. Feng, J. Geiger, M. Hirsch, U. Höfel, M. Jakubowski, T. Klinger, J. Knauer, G. Kocsis, A. Krämer-Flecken, M. Kubkowska, A. Langenberg, H. P. Laqua, N. Marushchenko, A. Mollén, U. Neuner, H. Niemann, E. Pasch, N. Pablant, L. Rudischhauser, H. M. Smith, O. Schmitz, T. Stange, T. Szepesi, G. Weir, T. Windisch, G. A. Wurden, D. Zhang, I. Abramovic, S. Äkäslompolo, A. Ali, J.Alcuson Belloso, P. Aleynikov, K. Aleynikova, R. Alzbutas, G. Anda, E. Ascasibar, J. Assmann, S.-G. Baek, J. Baldzuhn, M. Banduch, T. Barbui, M. Barlak, K. Baumann, W. Behr, C. Beidler, A. Benndorf, O. Bertuch, M. Beurskens, C. Biedermann, W. Biel, D. Birus, E. Blanco, M. Blatzheim, T. Bluhm, D. Böckenhoff, P. Bolgert, M. Borchardt, V. Borsuk, J. Boscary, H.-S. Bosch, L.-G. Böttger, R. Brakel, H. Brand, Ch. Brandt, T. Bräuer, H. Braune, S. Brezinsek, K.-J. Brunner, B. Brünner, R. Burhenn, R. Bussiahn, V. Bykov, Y. Cai, I. Calvo, B. Cannas, A. Cappa, A. Card, A. Carls, L. Carraro, B. Carvalho, F. Castejon, A. Charl, F. Chernyshev, M. Cianciosa, R. Citarella, Ł Ciupiński, G. Claps, M. J. Cole, F. Cordella, G. Cseh, A. Czermak, K. Czerski, M. Czerwinski, G. Czymek, A. da Molin, A. da Silva, G. Dammertz, A. de la Pena, S. Degenkolbe, P. Denner, T. Dittmar, C. P. Dhard, M. Dostal, M. Drevlak, P. Drewelow, Ph. Drews, A. Dudek, G. Dundulis, F. Durodie, P. van Eeten, G. Ehrke, M. Endler, D. Ennis, E. Erckmann, H. Esteban, T. Estrada, N. Fahrenkamp, J.-H. Feist, J. Fellinger, H. Fernandes, W. H. Fietz, W. Figacz, J. Fontdecaba, O. Ford, T. Fornal, H. Frerichs, A. Freund, M. Führer, T. Funaba, A. Galkowski, G. Gantenbein, Y. Gao, J.García Regaña, M. Garcia-Munoz, D. Gates, G. Gawlik, B. Geiger, V. Giannella, N. Gierse, A. Gogoleva, B. Goncalves, A. Goriaev, D. Gradic, M. Grahl, J. Green, A. Grosman, H. Grote, M. Gruca, O. Grulke, C. Guerard, P. Hacker, L. Haiduk, K. Hammond, X. Han, F. Harberts, J. H. Harris, H.-J. Hartfuß, D. Hartmann, D. Hathiramani, B. Hein, B. Heinemann, P. Heitzenroeder, S. Henneberg, C. Hennig, J.Hernandez Sanchez, C. Hidalgo, H. Hölbe, K. P. Hollfeld, A. Hölting, D. Höschen, M. Houry, J. Howard, X. Huang, M. Huber, V. Huber, H. Hunger, K. Ida, T. Ilkei, S. Illy, B. Israeli, A. Ivanov, S. Jablonski, J. Jagielski, J. Jelonnek, H. Jenzsch, P. Junghans, J. Kacmarczyk, T. Kaliatka, J.-P. Kallmeyer, U. Kamionka, R. Karalevicius, H. Kasahara, W. Kasparek, Y. Kazakov, N. Kenmochi, M. Keunecke, A. Khilchenko, C. Killer, D. Kinna, R. Kleiber, M. Knaup, A. Knieps, Th. Kobarg, F. Köchl, Y. Kolesnichenko, A. Könies, M. Köppen, J. Koshurinov, R. Koslowski, R. König, F. Köster, P. Kornejew, R. Koziol, M. Krämer, R. Krampitz, P. Kraszewsk, N. Krawczyk, T. Kremeyer, Th. Krings, J. Krom, M. Krychowiak, G. Krzesinski, I. Ksiazek, G. Kühner, T. Kurki-Suonio, S. Kwak, M. Landreman, R. Lang, S. Langish, H. Laqua, H. P. Laqua, R. Laube, S. Lazerson, C. Lechte, M. Lennartz, W. Leonhardt, L. Lewerentz, Y. Liang, Ch. Linsmeier, S. Liu, J.-F. Lobsien, D. Loesser, J.Loizu Cisquella, J. Lore, A. Lorenz, M. Losert, L. Lubyako, A. Lücke, A. Lumsdaine, V. Lutsenko, J. Maisano-Brown, O. Marchuk, M. Mardenfeld, P. Marek, S. Marsen, M. Marushchenko, S. Masuzaki, D. Maurer, K. McCarthy, P. McNeely, A. Meier, , and the W7-X Team. Magnetic configuration effects on the wendelstein 7-x stellarator. *Nature Physics*, 14(8):855–860, Aug 2018.

[10] E. Sánchez, J.L. Velasco, I. Calvo, and S. Mulas. A quasi-isodynamic configuration with good confinement of fast ions at low plasma beta. *Nuclear Fusion*, 63(6):066037, may 2023.

[11] J. L. Velasco, I. Calvo, E. Sánchez, and F. I. Parra. Robust stellarator optimization via flat mirror magnetic fields, 2023.

[12] R. Jorge, G.G. Plunk, M. Drevlak, M. Landreman, J.-F. Lobsien, K. Camacho Mata, and P. Helander. A single-field-period quasi-isodynamic stellarator. *Journal of Plasma Physics*, 88(5):175880504, 2022.

[13] Katia Camacho Mata, Gabriel G. Plunk, and Rogerio Jorge. Direct construction of stellarator-symmetric quasi-isodynamic magnetic configurations. *Journal of Plasma Physics*, 88(5):905880503, 2022.

[14] Alan Goodman, Katia Camacho Mata, Sophia A Henneberg, Rogerio Jorge, Matt Landreman, Gabriel Plunk, Hakan Smith, Ralf Mackenbach, and Per Helander. Constructing precisely quasi-isodynamic magnetic fields, 2022.

[15] A. Pytte and Allen H. Boozer. Neoclassical transport in helically symmetric plasmas. *The Physics of Fluids*, 24(1):88–92, 01 1981.

[16] Allen H. Boozer. Transport and isomorphic equilibria. *The Physics of Fluids*, 26(2):496–499, 02 1983.

[17] Matt Landreman and Elizabeth Paul. Magnetic fields with precise quasisymmetry for plasma confinement. *Phys. Rev. Lett.*, 128:035001, Jan 2022.

[18] F. Simon B. Anderson, Abdulgader F. Almagri, David T. Anderson, Peter G. Matthews, Joseph N. Talmadge, and J. Leon Shohet. The helically symmetric experiment, (hsx) goals, design and status. *Fusion Technology*, 27(3T):273–277, 1995.

[19] M C Zarnstorff, L A Berry, A Brooks, E Fredrickson, G-Y Fu, S Hirshman, S Hudson, L-P Ku, E Lazarus,

D Mikkelsen, D Monticello, G H Neilson, N Pomphrey, A Reiman, D Spong, D Strickler, A Boozer, W A Cooper, R Goldston, R Hatcher, M Isaev, C Kessel, J Lewandowski, J F Lyon, P Merkel, H Mynick, B E Nelson, C Nuehrenberg, M Redi, W Reiersen, P Rutherford, R Sanchez, J Schmidt, and R B White. Physics of the compact advanced stellarator ncsx. *Plasma Physics and Controlled Fusion*, 43(12A):A237, nov 2001.

[20] Viktor V. Nemov, Sergei V. Kasilov, Winfried Kernbichler, and Martin F. Heyn. Evaluation of $1/\nu$ neoclassical transport in stellarators. *Physics of Plasmas*, 6:4622–4632, 1999.

[21] J.L. Velasco, I. Calvo, F.I. Parra, and J.M. García-Regaña. Knosos: A fast orbit-averaging neoclassical code for stellarator geometry. *Journal of Computational Physics*, 418:109512, 2020.

[22] J.L. Velasco, I. Calvo, F.I. Parra, V. d'Herbemont, H.M. Smith, D. Carralero, T. Estrada, and the W7-X Team. Fast simulations for large aspect ratio stellarators with the neoclassical code knosos. *Nuclear Fusion*, 61(11):116013, sep 2021.

[23] Samuel Lazerson, John Schmitt, Caoxiang Zhu, Joshua Breslau, All STELLOPT Developers, and USDOE Office of Science. Stellopt, version 2.7.5, 5 2020.

[24] K. C. Shaing and J. D. Callen. Neoclassical flows and transport in nonaxisymmetric toroidal plasmas. *The Physics of Fluids*, 26(11):3315–3326, 11 1983.

[25] N. Nakajima, M. Okamoto, J. Todoroki, Y. Nakamura, and M. Wakatani. Optimization of bootstrap current in a large helical system with L = 2, August 1988.

[26] P. Helander, F. I. Parra, and S. L. Newton. Stellarator bootstrap current and plasma flow velocity at low collisionality. *Journal of Plasma Physics*, 83(2):905830206, 2017.

[27] M. Landreman, S. Buller, and M. Drevlak. Optimization of quasi-symmetric stellarators with self-consistent bootstrap current and energetic particle confinement. *Physics of Plasmas*, 29(8), 08 2022. 082501.

[28] Zhichen Feng, David A. Gates, Samuel A. Lazerson, Matt Landreman, Neil Pomphrey, and GuoYong Fu. Optimization of quasi-axisymmetric stellarators with varied elongation. *Physics of Plasmas*, 27(2):022502, 02 2020.

[29] A. Bañón Navarro, A. Di Siena, J.L. Velasco, F. Wilms, G. Merlo, T. Windisch, L.L. LoDestro, J.B. Parker, and F. Jenko. First-principles based plasma profile predictions for optimized stellarators. *Nuclear Fusion*, 63(5):054003, mar 2023.

[30] M. Barnes, I. G. Abel, W. Dorland, T. Görler, G. W. Hammett, and F. Jenko. Direct multiscale coupling of a transport code to gyrokinetic turbulence codesa). *Physics of Plasmas*, 17(5):056109, 04 2010.

[31] W. I. van Rij and S. P. Hirshman. Variational bounds for transport coefficients in three-dimensional toroidal plasmas. *Physics of Fluids B: Plasma Physics*, 1(3):563–569, 1989.

[32] M. Landreman, H. M. Smith, A. Mollén, and P. Helander. Comparison of particle trajectories and collision operators for collisional transport in nonaxisymmetric plasmas. *Physics of Plasmas*, 21(4):042503, 2014.

[33] P Helander and DJ Sigmar. *Collisional transport in magnetized plasmas*. Cambridge university press, 2005.

[34] S. P. Hirshman, K. C. Shaing, W. I. van Rij, C. O. Beasley, and E. C. Crume. Plasma transport coefficients for nonsymmetric toroidal confinement systems. *The Physics of Fluids*, 29(9):2951–2959, 1986.

[35] Matt Landreman. The monoenergetic approximation in stellarator neoclassical calculations. *Plasma Physics and Controlled Fusion*, 53(8):082003, jun 2011.

[36] Lloyd N. Trefethen and J. A. C. Weideman. The exponentially convergent trapezoidal rule. *SIAM Review*, 56(3):385–458, 2014.

[37] E. Anderson, Z. Bai, C. Bischof, S. Blackford, J. Demmel, J. Dongarra, J. Du Croz, A. Greenbaum, S. Hammarling, A. McKenney, and D. Sorensen. *LAPACK Users' Guide*. Society for Industrial and Applied Mathematics, Philadelphia, PA, third edition, 1999.

[38] J. L. Tennyson, John R. Cary, and D. F. Escande. Change of the adiabatic invariant due to separatrix crossing. *Phys. Rev. Lett.*, 56:2117–2120, May 1986.